ARL-TR- 7962 ● MAR 2017

US Army Research Laboratory

Morphological Characterization of the Frontal and Parietal Bones of the Human Skull

by Stephen L Alexander
SURVICE Engineering Company, Belcamp, MD

Karin Rafaels
Survivability/Lethality Analysis Directorate, ARL

C Allan Gunnarsson and Tusit Weerasooriya
Weapons and Materials Research Directorate, ARL

NOTICES

Disclaimers

The findings in this report are not to be construed as an official Department of the Army position unless so designated by other authorized documents.

Citation of manufacturer's or trade names does not constitute an official endorsement or approval of the use thereof.

Destroy this report when it is no longer needed. Do not return it to the originator.

ARL-TR- 7962 ● MAR 2017

US Army Research Laboratory

Morphological Characterization of the Frontal and Parietal Bones of the Human Skull

by Stephen L Alexander
SURVICE Engineering Company, Belcamp, MD

Karin Rafaels
Survivability/Lethality Analysis Directorate, ARL

C Allan Gunnarsson and Tusit Weerasooriya
Weapons and Materials Research Directorate, ARL

REPORT DOCUMENTATION PAGE

Form Approved
OMB No. 0704-0188

1. REPORT DATE *(DD-MM-YYYY)*	2. REPORT TYPE	3. DATES COVERED (From - To)
March 2017	Technical Report	October 2015–December 2016

4. TITLE AND SUBTITLE
Morphological Characterization of the Frontal and Parietal Bones of the Human Skull

5a. CONTRACT NUMBER
W911QX-16-D-0014

5b. GRANT NUMBER

5c. PROGRAM ELEMENT NUMBER

6. AUTHOR(S)
Stephen L Alexander, Karin Rafaels, C Allan Gunnarsson, Tusit Weerasooriya

5d. PROJECT NUMBER

5e. TASK NUMBER

5f. WORK UNIT NUMBER

7. PERFORMING ORGANIZATION NAME(S) AND ADDRESS(ES)
US Army Research Laboratory
ATTN: RDRL-WMP-B
Aberdeen Proving Ground, MD 21005-5066

8. PERFORMING ORGANIZATION REPORT NUMBER
ARL-TR-7962

9. SPONSORING/MONITORING AGENCY NAME(S) AND ADDRESS(ES)

10. SPONSOR/MONITOR'S ACRONYM(S)

11. SPONSOR/MONITOR'S REPORT NUMBER(S)

12. DISTRIBUTION/AVAILABILITY STATEMENT
Approved for public release; distribution unlimited.

13. SUPPLEMENTARY NOTES

14. ABSTRACT
Bone specimens were collected from the frontal and parietal bones of 4 adult, human skulls. The microstructure was characterized using micro-tomography (CT) at about 6-μm resolution to map the change of porosity as a function of the depth, P(d), from the inner surface nearest to the brain to the outer surface nearest to the skin. A quantifiable method was developed using the measured P(d) to objectively distinguish between the 3 layers of the skull: the outer table, diploë, and inner table. The thickness and average porosity of each of the layers were then calculated from the measured porosity distributions. A Gaussian function was used to represent the P(d) curves. The Gaussian parameters were identified through least squares, and the values indicated the peak porosity and the relative thickness of the diploë. The results for total thickness, the thickness and average porosity of each of the layers, and the Gaussian parameters were compared between the 2 bone types (frontal and parietal), while accounting for skull-to-skull variability. The primary differences were that parietal bones generally had a larger diploë accompanied by a thinner inner table. The arrangement of the porous vesicular structure within the outer table was also obtained with micro-CT scans with longer scan times, using enhanced parameters for higher resolution and lower noise in the images. From these scans, the porous structure of the bone appeared to be randomly arranged in the transverse plane, compared to the porous structure of the human femur, which is aligned in the loading direction.

15. SUBJECT TERMS
human skull, skull morphology, micro-CT, skull mechanics, micro-tomography

16. SECURITY CLASSIFICATION OF:			17. LIMITATION OF ABSTRACT	18. NUMBER OF PAGES	19a. NAME OF RESPONSIBLE PERSON
a. REPORT	b. ABSTRACT	c. THIS PAGE			Carey Gunnarsson
Unclassified	Unclassified	Unclassified	Unclassified	78	19b. TELEPHONE NUMBER (Include area code) 410.306.0990

Standard Form 298 (Rev. 8/98)
Prescribed by ANSI Std. Z39.18

Contents

List of Figures

List of Tables

Preface

The research reported in this document was performed in connection with contract W911-QX-14-C0016 and W911QX-16-D-0014 with the US Army Research Laboratory. The views and conclusions contained in this document are those of TKC Global Inc., SURVICE Engineering Company, and the US Army Research Laboratory. Citation of manufacturer's or trade names does not constitute an official endorsement or approval of the use thereof. The US Government is authorized to reproduce and distribute reprints for Government purposes notwithstanding any copyright notation hereon.

Acknowledgments

The authors would like to acknowledge the contributions of Gajanan Deshmukh (US Army Aberdeen Test Center), who assisted in postprocessing the specimen micrographs, and Ann Mae DiLeonardi (US Army Research Laboratory) for help with specimen extraction.

1. Introduction

One of the primary functions of the skull is to protect the brain from mechanical insults. In the human case, the brain is protected by the calvarium, which consists of 4 bones joined together by sutures: the frontal bone, the 2 parietal bones on the sides, and the occipital bone toward the rear. The cross-sectional profile of these cranial bones is organized in a sandwich structure of 3 layers. The outer and inner tables are made of dense cortical bone, and the middle layer, also known as the diploë, is porous trabecular bone.

Understanding the mechanical response of these bones with sandwich structure to externally applied mechanical loading aids the design and evaluation of head protection equipment and strategies. The mechanical properties of bone are strongly correlated to bone-volume-fraction (fbv), or its complement, porosity (1 - fbv). A power-law relationship between the apparent modulus of bone and the fbv has been extensively developed in the literature, as reviewed by Helgason et al. (2008). This apparent modulus describes the far-field response of the overall structure of bone, and it has been shown to depend on the fbv raised to an exponential factor falling in the range between 2 and 3 (Carter and Hayes 1977; Goulet et al. 1994; Alexander et al. 2016). However, these results have been almost exclusively developed for bones without the sandwich structure of the skull, such as the femur, vertebra, and tibia (Helgason et al. 2008). The subdivision of the cranial thickness (or depth) into 3 distinct layers with a rapidly changing porosity profile challenges the use of a single modulus-porosity relationship to describe the mechanical response of the skull.

An early study on modulus-density relationships in the skull was by McElhaney et al. (1970). In this pioneering work, the compression modulus of human skull loaded normal to the outer surface was approximated by a function of the third power of the porosity (porosity to the power of 3). More recently, the authors of the present report used the concept of the power-law relationship between modulus and bone volume fraction to describe localized, depth-dependent mechanical properties of animal cranial bone (Alexander et al. 2016). In this work, the deformation response of the various sections of the cranial bone in response to loading was visualized and quantified (quantitative-visualization), and shown to vary through the thickness of the skull from the inner to outer surface. In addition, the variation of the fbv along the thickness was also measured. Finally, the change of apparent modulus through the thickness was calculated by relating the gradient in deformation (strain) to the fbv gradient.

However, the ability of a similar power-law relationship to account for the localized properties of the human skull would depend on the structure of human cranial bone, which is not well known. Several aspects of the skull morphology must be investigated before relating the modulus with the depth. First, the change of porosity through the thickness of the human cranial bone must be quantified. Then, any differences in these porosity changes between the various bones of the calvarium must be identified. Moreover, aligned microstructures within the skull (structural anisotropy) could imply directional dependence in the mechanical response (mechanical anisotropy). Mechanical anisotropy would need to be accounted for if a directional dependence is present, since approximating the modulus from only the porosity assumes that the relevant microstructure is randomly arranged (structural isotropy), without preferential alignment. As far as we know, these details of the human skull morphology have not been fully addressed in the existing literature.

Several authors have quantified the thickness of the 3 layers of the human skull (McElhaney et al. 1970; Fry and Barger 1978; Peterson and Dechow 2002, 2003; Lynnerup et al. 2005; Sabanciogullari et al. 2013; Huang et al. 2015). However, previous reports of layer thicknesses have generally relied on qualitative methods of layer identification and segregation, which are not ideal. For example, the inconsistency of the porosity in the diploë has challenged the use of qualitative methods for delineation between layers, making layer identification either difficult or impossible in some regions of the skull (Lynnerup et al. 2005; Huang et al. 2015; Lillie et al. 2016). Furthermore, these methods have also led to subjectivity in the identification of the layer boundaries, which is likely responsible for the large amount of variations that are reported in literature (Boruah et al. 2015). Only a few recent studies have presented quantitative methods for layer segregation, resulting in repeatable results (Boruah et al. 2013; Boruah et al. 2015; Lillie et al. 2015). One method identified the diploë by the onset of pixels corresponding to porous space within specified regions of the image stack (Boruah et al. 2013; Boruah et al. 2015) while another used a full-width-half-max analysis of the X-ray attenuation through the thickness of the specimen (Lillie et al. 2015).

The porosity (porous-volume-fraction) of human cranial bone has only been reported as an average over the entire thickness of the skull that includes all 3 layers (Rahmoun et al. 2014), or for each layer as an average within that layer (Boruah et al. 2013; Boruah et al. 2015). McElhaney et al. (1970) was an exception in considering the depth-dependence of the porosity. This study suggested that the through-thickness variation of porosity could be described by a 1-term Gaussian function: a bell-shaped curve with the porosities lowest in the tables and peaking in the diploë. However, this use of the Gaussian function to approximate the through-

thickness porosity variation was motivated only by observation of the porosity distribution from serial sections, using a technique that was not detailed in the paper (McElhaney et al. 1970).

Finally, the extent of structural anisotropy in the transverse plane of the skull, parallel to the outer surface, is unclear. In the extensively studied load-bearing cortical part of long bones, such as the femur, microstructure is aligned in the direction of anatomical loading along the long axis (Peyrin et al. 2000) and mechanical properties are transversely isotropic at mesoscale. These microstructural subelements are called osteons, and consist of a cylindrical pore in the center, called the Haversian canal, which is encircled by lamella reinforced with collagen-mineral fibrils. While the outer and inner tables of cranial bone are known to contain osteons (Trammell 2012), the alignment of these osteons and other microstructural details have not been conclusively determined or reported in literature. Some degree of directional dependence in the transverse plane has been found from mechanical characterization of the outer table, thereby indicating the presence of anisotropy (Peterson and Dechow 2003). However, evidence of consistent directional dependencies in human skulls is not present in literature.

The preset study used high-resolution microcomputed tomography (micro-CT) to quantify the change of porosity through the thickness from the outer to the inner surface, through the diploë. Gaussian functions were optimized to describe the high-resolution porosity measurements, and a systematic method for differentiating between the 3 microstructural layers was developed. The porosity and thickness ratios of the 3 layers were then calculated. The results were compared between skulls and bone types to determine any systematic variation between the different bones of the skulls, while accounting for the random skull-to-skull variation. Finally, the 3-dimensional arrangement of the vesicular structure within the outer table was visualized using higher resolution micro-CT. The visual results were used to identify the extent of structural alignment within the dense part of the skull bone structure.

2. Methods

2.1 Specimen Extraction

Bone specimens originated from the skulls of 4 fresh (nontreated) and frozen, male postmortem human subject (PMHS) donors aged 76–86 yrs. The skulls did not have a history of musculoskeletal diseases nor did they demonstrate any macroscopic pathological changes near the specimen extraction sites.

Sections of the frontal and parietal bones were retrieved from the skulls using a handheld bone saw after all soft tissues had been removed.

Nine specimens were then collected from each section of the skull. The sets of 9 specimens formed a square grid, as depicted in the example given in Fig. 1. The location of the grid on the skull was recorded prior to each extraction with 2 measurements, which localized the center of the grid. The measurement marked as C in Fig. 1 was from the center of the grid to the coronal suture. The coronal suture separates the frontal bone, which is anterior to (in front of) the suture, from the 2 parietal bones, posterior to (behind) the suture. The measurement marked as S in Fig. 1 was from the center of the grid to the anteroposterior midline, which divides the skull into left and right sides. This midline was identified by the sagittal suture, which lies posterior to the coronal suture. The sagittal suture was also manually extrapolated to the frontal bone to measure S for extraction grids from frontal bones.

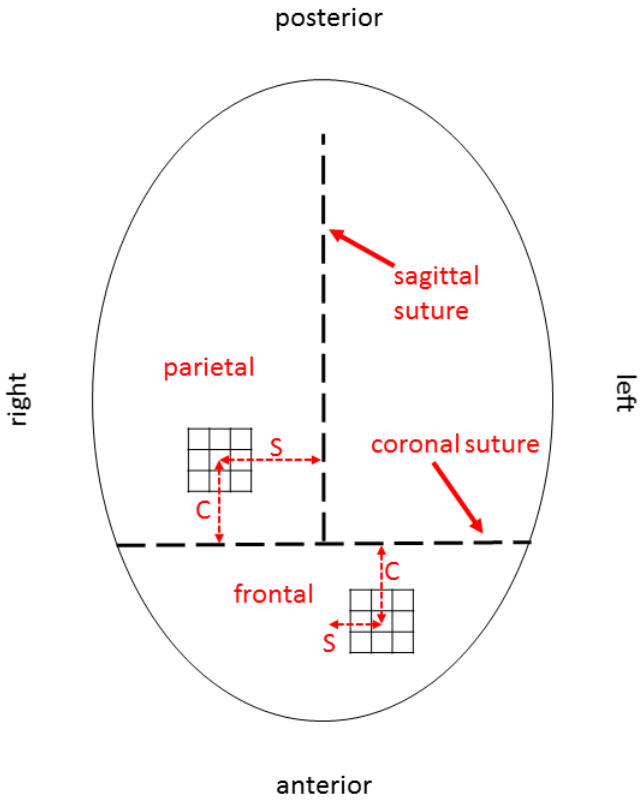

Fig. 1 Schematic of the human skull, viewed from above. The locations of the specimen grids are shown on the frontal and parietal bones. Distances from the grid centers to the coronal suture and midline (sagittal suture) are depicted by C and S, respectively. Note: the parietal grid is shown on the right parietal bone only as an example. For some skulls, the parietal grid originated from the left parietal bone, as listed in Table 1.

Table 1 PMHS sample information

Skull no. *(AA)*	Age (yrs)	Weight (kg)	Stature (cm)	Bone	Specimen no. range *(BB)*	Distance from midline (cm)	Distance from coronal suture (cm)
04	79	72	177	Frontal	01 to 09	0	–3.6
				Parietal (R)	10 to 18	6.4	3.8
06	83	63	175	Frontal	01 to 09	0	6.5
. . .	. . .	. . .	. . .	Parietal (L)	19 to 27	–5.9	–5.2
07	86	66	172	Frontal	10 to 18	–2	6.6
10	76	54	182	Frontal	01 to 09	0	6.1
. . .	. . .	. . .	. . .	Parietal (R)	10 to 18	5.6	–3.4

Note: Parietal bones on the left (L) and right (R) side of the skull are separately identified. Distances are listed from the center of the grid. Negative distances from the coronal sutures indicate that the grid was posterior to (behind) the suture. Negative distances from the midline indicate the grid was to the left of the midline.

Each of the specimens was catalogued with an AA-BB label, in which AA was the skull number (04, 06, 07, or 10) and BB was the unique number of the specimen within each skull (ranging from 01 to 27). The BB numbering scheme is shown for each bone in Fig. 2. For the purposes of this report, the term superior refers to the top of the head (farthest from the shoulders) and inferior refers to the bottom of the head (toward the shoulders).

The specimens were cut from the bone sections using a diamond-coated bone pathology saw (Exact 312, Exact Technologies, Inc.) with continual irrigation to reduce any damage due to heating. Extracted specimens were approximately rectangular parallelepipeds, with dimensions on the outer surfaces of 8 × 8 mm. The specimens included the entire thickness of the skull, with both outer and inner surfaces left intact. The thickness of the specimen was the distance measured from the inner surface, closest to the brain, to the outer surface, closest to the skin. The thickness will also be referred to as the depth dimension in this report. The term specimen(s) will be used throughout this report to refer to these individual specimens extracted from the skull.

After extraction, each specimen was immersed in Hanks Buffered Saline Solution (HBSS) and stored in an individual vial. Vials were kept at 4 °C when the specimen was not actively used for morphological characterization.

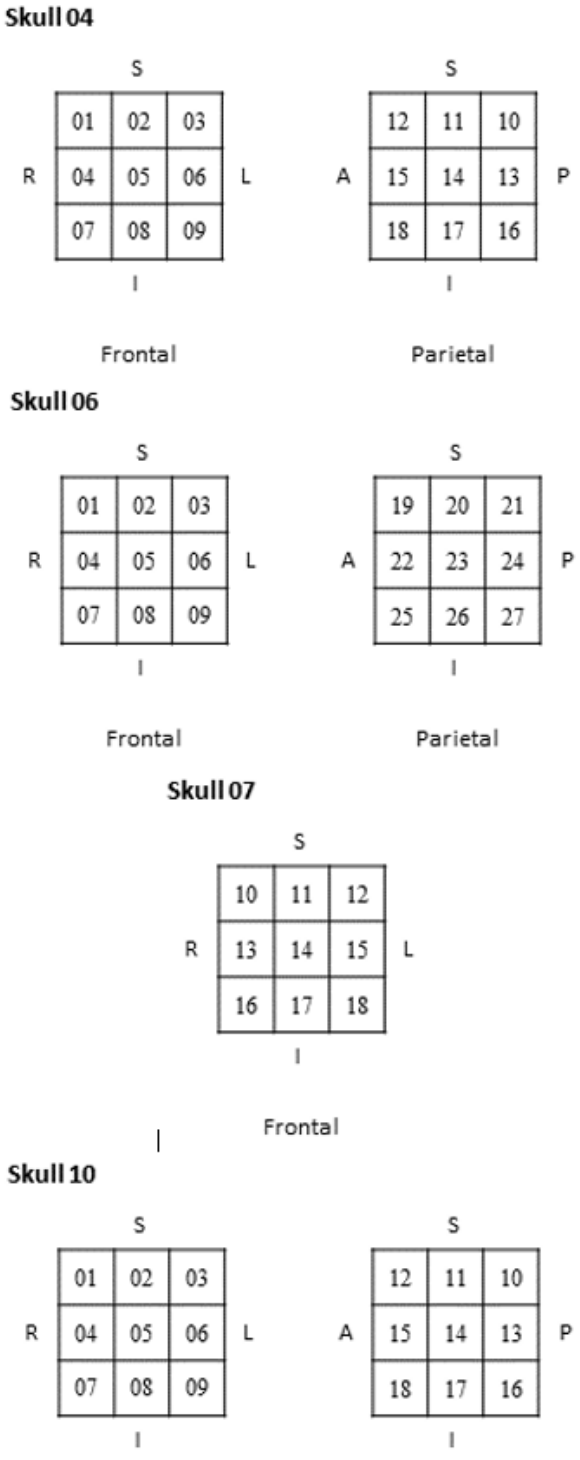

Fig. 2 BB numbering scheme for each specimen extraction grid from each skull. Markings outside the grid indicate in-situ orientation: superior (S, toward the top of the skull), inferior (I, toward the base of the skull), anterior (A, toward the front of the skull), posterior (P, toward the rear of the skull), right (R), and left (L).

2.2 Microcomputed Tomography

Prior to imaging, specimens were removed from storage, wrapped in HBSS-soaked gauze, and placed in a small vial to be mounted in the scanner. The vial was also filled with HBSS.

The specimens were imaged using a micro-CT scanner (Skyscan 1172, Bruker micro-CT), with scanning parameters designated by 1 of the 4 different sets listed in Table 2. For all 4 sets, micro-CT scans were performed at 62 kV and 161 mA while using a 0.5-mm aluminum filter. The use of different scanning parameters was necessitated by external circumstances related to the scanner. Parameters were chosen to balance the competing needs to minimize the electrical and image noise, while also minimizing the time required to scan each specimen. The effect of the different scanning parameters on the quantitative data was further investigated in Appendix A. The results indicated that the variability in measured parameters from micro-CT images were relatively small for the range and combinations of parameters given in Table 2.

Table 2 Scanning parameters

Parameter set (no.)	Resolution/voxel size (µm)	Frame avg. (no. of frames)	Rotation step (°)	Random movement	Approx. scan time (h)
1	6.7	10	0.2	5	12
2	6.1	10	0.2	20	13
3	5.3	12	0.1	20	18
4	5.3	10	0.15	20	10.5

An image stack was reconstructed from the initial micro-CT scan. It was rotated using DataViewer software (Bruker micro-CT) so that the normal at the center of the outer table was aligned in the vertical direction, as shown in Fig. 3. After rotation, each image of the stack represented a 1-voxel-thick horizontal slice of the specimen. In this report, the image plane will also be referred to as the transverse plane. The error associated with stack rotation was quantified in Appendix A and shown to be negligible.

After rotation, the voxels corresponding to the specimen were selected by creating the volume of interest (VOI) within CTAn Software (Bruker micro-CT). The VOI of individual specimens were independently identified, as each specimen had different overall dimensions. The first step in creating the VOI was to select the images corresponding to the top and bottom of the specimen, which bounded the VOI. These bounds were selected in the following manner. The operator started

at the top of the image stack, above the specimen. The images in this region did not contain any bone. Then, the image stack was traversed down toward the center of the specimen until reaching an image containing the full perimeter of the specimen. This image was well below the outer surface. The full specimen perimeter was noted. The image stack was then traversed upward, toward the outer surface, until the area corresponding to bone was 50% of the specimen area identified from the image with the full perimeter. This image with the 50% bone area was selected as the "top" of the specimen. The "bottom" of the specimen was selected in a similar manner. The operator started from an image slice far below the specimen. The image stack was traversed up toward the center until reaching an image with the full specimen perimeter. Finally, the image stack was again traversed down toward the inner surface, and the last image for which the specimen area was occupied by at least 50% bone was selected as the "bottom" of the specimen.

Each of the transverse images within the stack contained both the specimen area and voxels corresponding to the media encompassing the specimen. Therefore, after identifying the top and bottom VOI bounds, the operator then demarcated the boundary of the specimen within the transverse images. The boundary was manually traced using the polygonal region of interest (ROI) tool. These polygonal ROIs were created on several image slices within the top and bottom VOI bounds. The ROIs for the remaining images were automatically created from the manually traced polygons using interpolation (CTAn software). Finally, the operator inspected visually all of the VOI images to ensure that the combination of ROIs over all of the slices encapsulated the specimen. The process was iterated to correct the ROIs as needed.

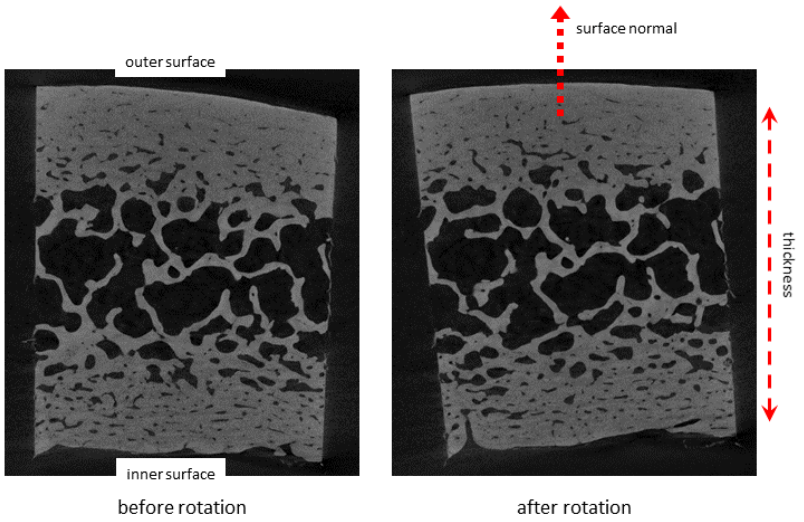

Fig. 3 Example of the rotation applied to the image stack in DataViewer such that the normal at the center of the outer table was in the vertical direction. Images shown are through-thickness and are from Specimen 04-03.

After VOI creation, images were filtered using a Gaussian blur ($\sigma = 1.5$) to reduce noise. Images were then binarized using the 3-D Otsu algorithm (Otsu 1975), constrained to the VOI.

2.3 Summary of Terminology Used

Table 3 provides a summary of terms introduced in the preceding sections, which are relevant to the image analysis procedures and specimen identification.

Table 3 Terminologies

Term	Description
Extraction	
Specimen	The individual coupons collected from the skulls for analysis and catalogued with an *AA-BB* label.
Skull layers/sections	Refers to the 3 layers that comprise the sandwich structure of the adult human skull: outer table, diploë, and inner table.
Extraction grid	The grid of 9 specimens extracted from each bone. The arrangement of each grid within a rectangular section of the skull was shown in Fig. 2
Bone type	Frontal or parietal (Fig. 1)
Imaging and Analysis	
Thickness/depth	The dimension that spans from the inner surface to the outer surface of the specimens
Transverse plane	The plane corresponding to the images, perpendicular to the normal of the outer surface of the specimen
ROI	The region of interest of each image in the micro-CT stack, selected so as to contain the transverse planes of the specimen
VOI	The 3-D volume of interest of the micro-CT stack, selected so as to separate the specimen from the surrounding media

2.4 Statistical Analysis

Three different pooling methods were used to average the various parameters that were calculated from each individual specimen. First, the parameters were averaged only over each extraction grid. This produced 7 averages: for different bone types (parietal and frontal) of each skull (04, 06, 07, and 10). Then, results were pooled for each bone type, regardless of its skull origin. This gave 2 averages, one for frontal and the other for parietal. Finally, results were pooled by skull of origin, regardless of bone type. This procedure gave 3 averages, for Skulls 04, 06, and 10. No such pooling by skull origin was needed for Skull 07 because only one bone type (frontal) was scanned from this skull.

Two-way analysis of variance (ANOVA) and posthoc tests were used to further quantify the relative effect of 2 sources of variation: bone type (frontal, parietal) and skull origin (Skull 04, Skull 06, or Skull 10). These tests did not include results from Skull 07, since only the frontal bone was studied from this skull. Statistical analysis was carried out using JMP software (JMP 12.0.1, SAS Institute). Statistical difference was determined at a 95% confidence level ($p < 0.05$). Differences between the results pooled by bone type (parietal and frontal) were calculated with Student's t-test. For all other groups, differences were calculated using Tukey's Honestly Significant Difference (HSD) test.

3. Results

3.1 Representative Images from Each Extraction Grid

Representative specimens from the 2 types of bone (parietal and frontal) were selected for each skull. Figures 4–6 show 2 different types of images for each of these specimens. The through-thickness image shows the whole depth dimension, from the inner, brain-most, surface of the bone to the outer, skin-most, surface of the bone. Various cross-sectional images are also included at various depths. The cross-sectional images correspond to image slices roughly perpendicular to the normal at the center of the outer surface of the skull.

Figure 4 shows a through-thickness image of Specimen 04-02 with cross-sectional images of each of the 3 sections: outer table, diploë, and inner table. Figures 5 and 6 show through-thickness images from the remaining bones, accompanied by a cross-sectional image of the diploë.

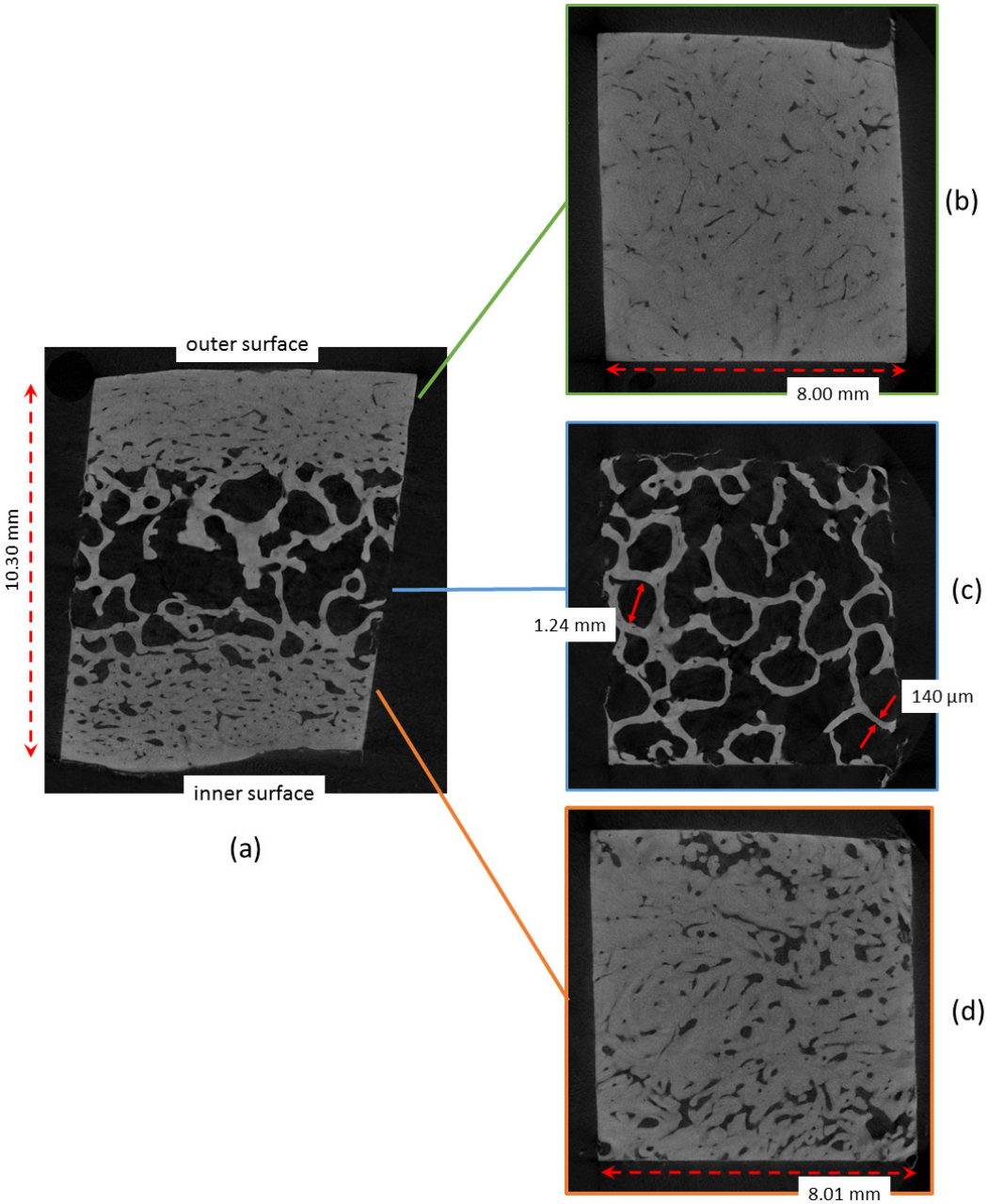

Fig. 4 Through-thickness image of Specimen 04-02 (a), and cross-sectional images of the outer table (b), diploë (c), and inner table (d)

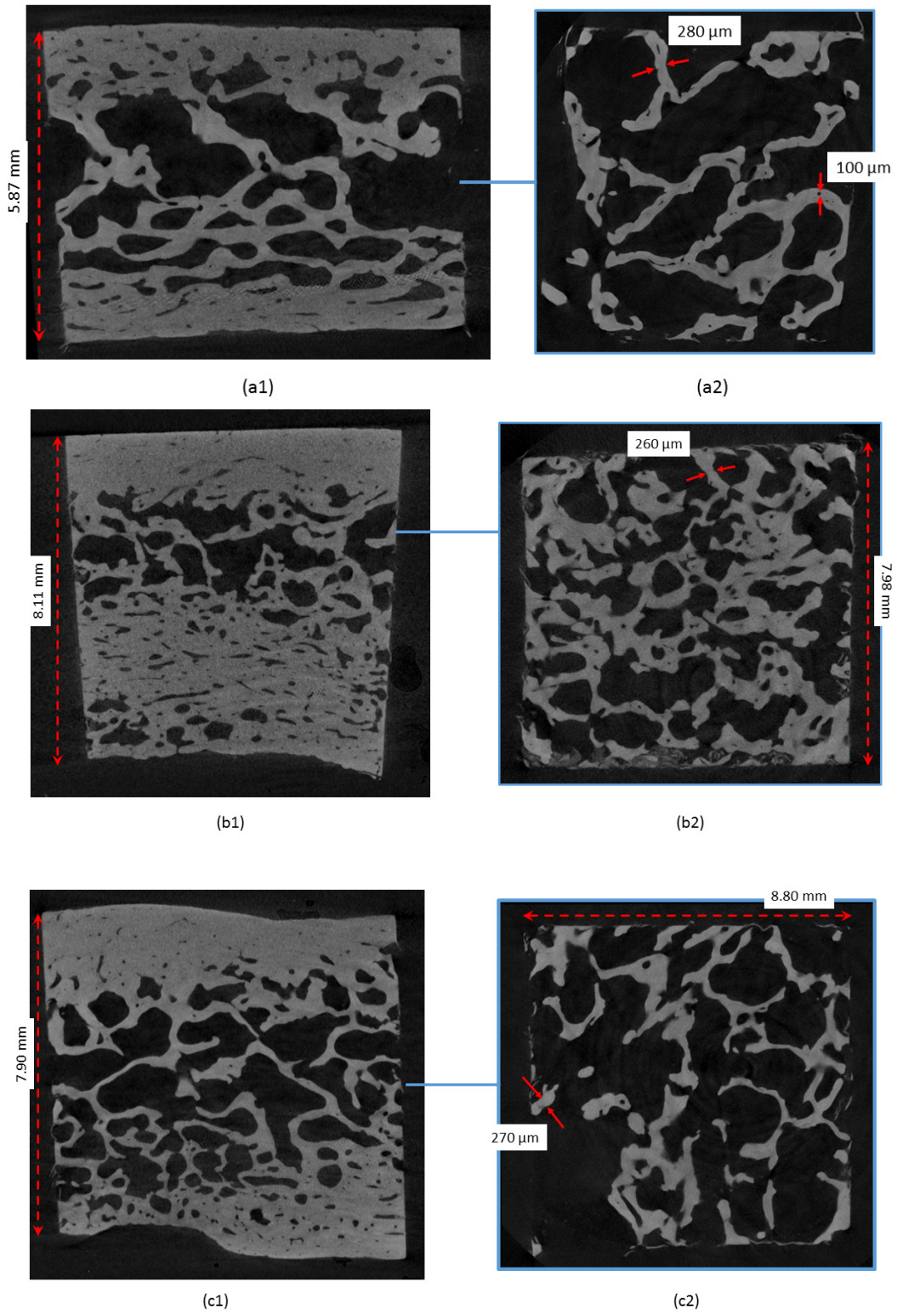

Fig. 5 Representative images from each bone section. Through-thickness images are on the left and cross-sectional images of the diploë are on the right. The bones are (a) 04-14, (b) 06-06, and (c) 06-26.

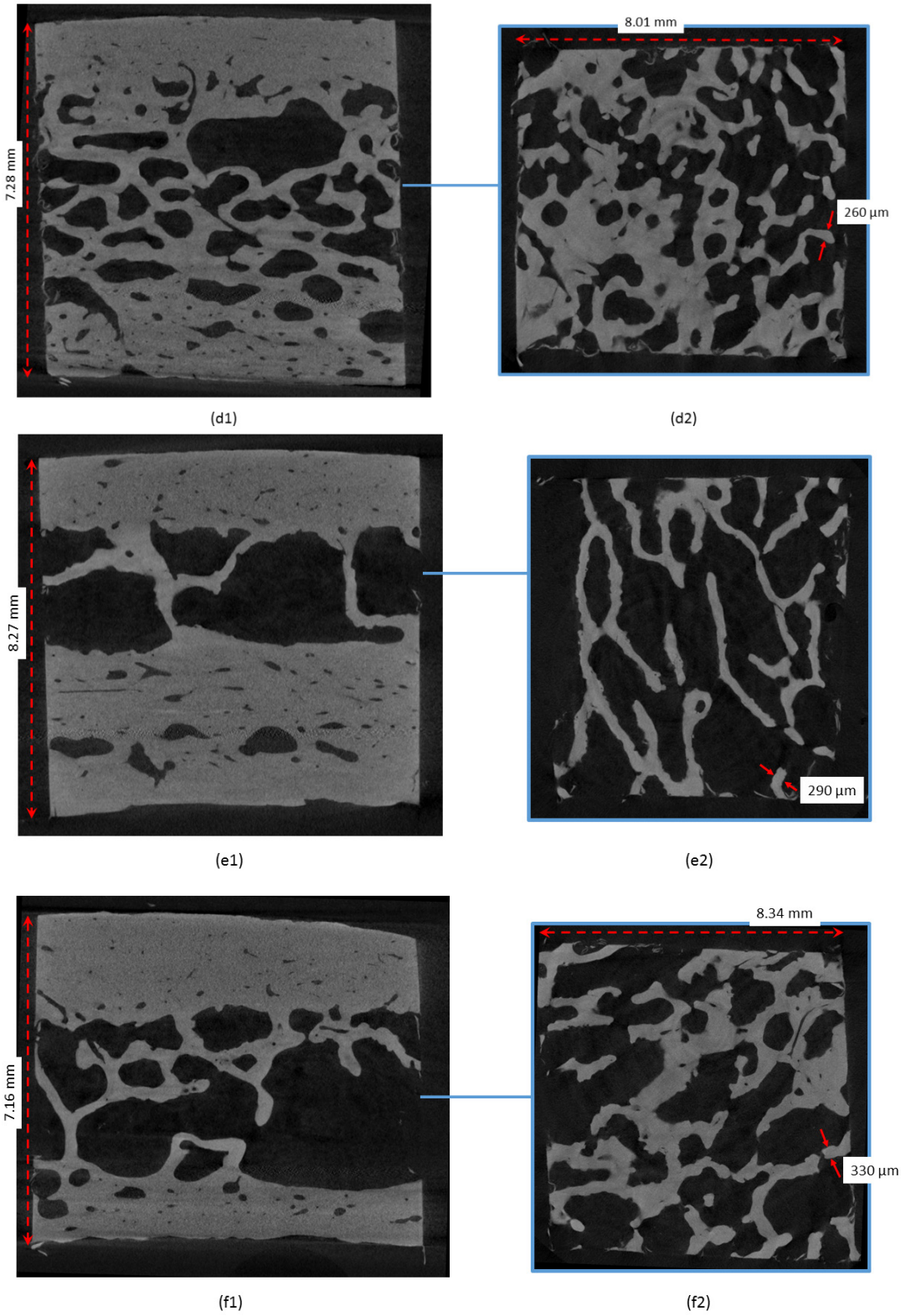

Fig. 6 Representative images from each bone section. Through-thickness images are on the left and cross-sectional images of the diploë are on the right. The bones are (d) 07-10, (e) 10-04, and (f) 10-17.

3.2 Outer Table, Diploë, and Inner Table Layer Identification and Thickness Measurements

The porosity of each binarized image within a given stack was calculated as the fraction of the porous area to the total area of the image. The result described the porosity as a function of depth, *P(d)*, from the inner surface to the outer surface of the specimen. An example is given in Fig. 7.

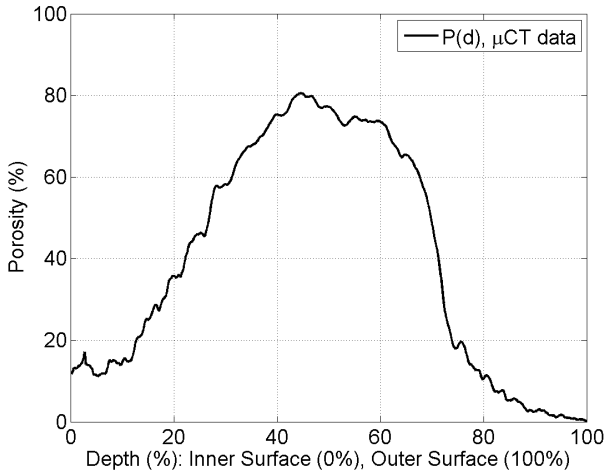

Fig. 7 Porosity as a function of depth, *P(d),* for Specimen 04-03

The overall thickness of the entire specimen, t, was measured from the size of the micro-CT image stack (VOI, as described in Section 2.2). The size in pixels was converted to millimeters based on the isotropic voxel size (Table 2). Next, the thicknesses of the outer table, diploë, and inner table were calculated as t_o, t_d, and t_i, respectively. Section thicknesses were calculated directly from the porosity-depth profile derived from the micro-CT measurements, *P(d)*. The procedure started at the outer surface, d = 100%, where the porosity was always less than 30%. The depth d was then decreased until *P(d)* > 30%. The first depth, d, for which *P(d)* > 30%, was taken as the transition from the outer table to the diploë. Then, the depth was further decreased toward d = 0% (the inner surface). The next depth, d, for which *P(d)* again fell below 30% was taken as the transition boundary from the diploë to the inner table.

Figure 8 shows a schematic of this process of identifying the 3 sections. The process was based on a cutoff threshold of the porosity percentage to have repeatable results. This method offered an improvement over the subjective analysis used in literature.

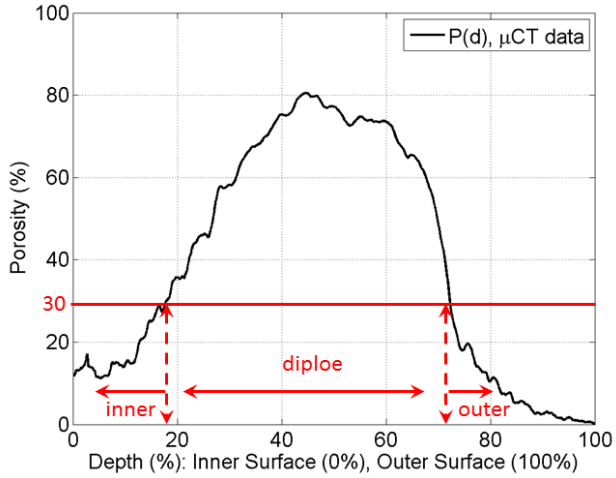

Fig. 8 Procedure to determine the outer table, diploë, and inner table thicknesses from the porosity-depth profile. This example uses the porosity-depth profile of Specimen 04-03 (Fig. 7).

The cutoff porosity percentage of 30% was chosen because the outer and inner tables are consistently considered as cortical bone, while the diploë is considered trabecular bone. Secondly, cortical bone has been described as bone with porosity of less than 30%, while trabecular bone has porosity greater than 30% (Mow and Huiskes 2005).

Figures 9–12 show the mean and standard deviation of the 4 parameters: t, t_o, t_d, and t_i averaged over each extraction grid. Tables 4–7 list the extraction grid averages. The tables also list the average over each skull (Skull 4, Skull 6, and Skull 10) and the average over each bone type (frontal, parietal). The tables indicate which groups are statistically different ($p < 0.05$, Section 2.4). Appendix C contains box plots of the 4 thickness parameters: t, t_o, t_d, and t_i.

Two-way ANOVA (Section 2.4) indicated that both skull origin and bone type had a significant effect for all 4 of these parameters ($p < 0.05$). The interaction effect between skull origin and bone type was only significant for t and t_i. Appendix C contains results for the thickness in millimeters of each of the 3 layers of the skull (outer table, diploë, and inner table), calculated for each extraction grid and grouping.

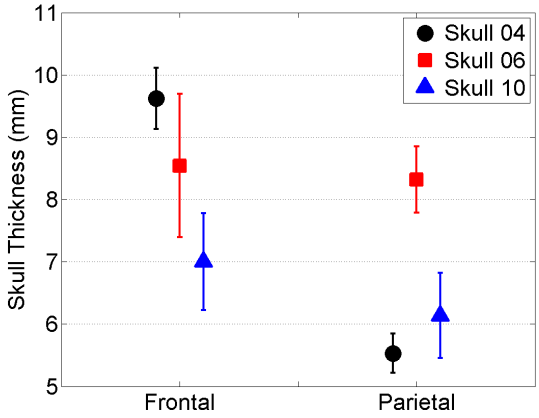

Fig. 9 Average values of the overall skull thickness, *t*

Table 4 Total skull thickness, *t*

Grouping	mean ± std	Connecting symbols
Skull 04, frontal	9.6 ± 0.5	*
Skull 06, frontal	8.5 ± 1.1	#
Skull 06, parietal	8.3 ± 0.5	#
Skull 10, frontal	7.0 ± 0.8	@
Skull 10, parietal	6.1 ± 0.7	@ &
Skull 04, parietal	5.5 ± 0.3	&
Skull 06, pooled	8.4 ± 0.9	¶
Skull 04, pooled	7.6 ± 2.1	◀
Skull 10, pooled	6.6 ± 0.8	Δ
Frontal, pooled	8.4 ± 1.4	^
Parietal, pooled	6.7 ± 1.3	$

Note: Results are reported in units of millimeters. Groups that do not share the same symbol in the Connecting symbols column are significantly different.

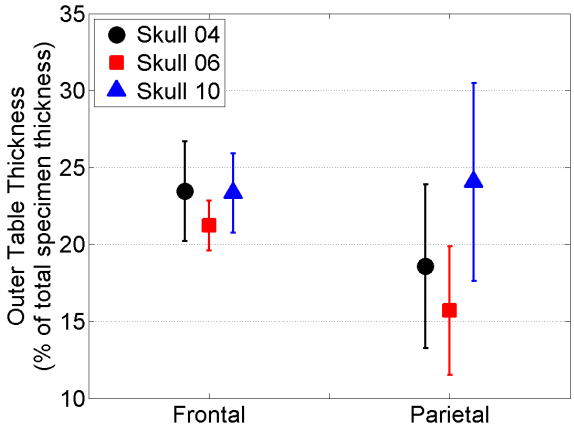

Fig. 10 Average values of the thickness percentage of the outer table, t_o

Table 5 Relative outer table thickness percentage, t_o

Grouping	mean ± std	Connecting symbols
Skull 10, parietal	24.1 ± 6.4	*
Skull 04, frontal	23.5 ± 3.2	*
Skull 10, frontal	23.3 ± 2.6	*
Skull 06, frontal	21.2 ± 1.6	* #
Skull 04, parietal	18.6 ± 5.3	* #
Skull 06, parietal	15.7 ± 4.2	#
Skull 10, pooled	23.7 ± 4.8	¶
Skull 04, pooled	21.0 ± 5.0	¶ ◄
Skull 06, pooled	18.5 ± 4.2	◄
Frontal, pooled	22.7 ± 2.7	^
Parietal, pooled	19.4 ± 6.3	$

Note: Results are reported in units of thickness percentage (%). Groups that do not share the same symbol in the Connecting symbols column are significantly different.

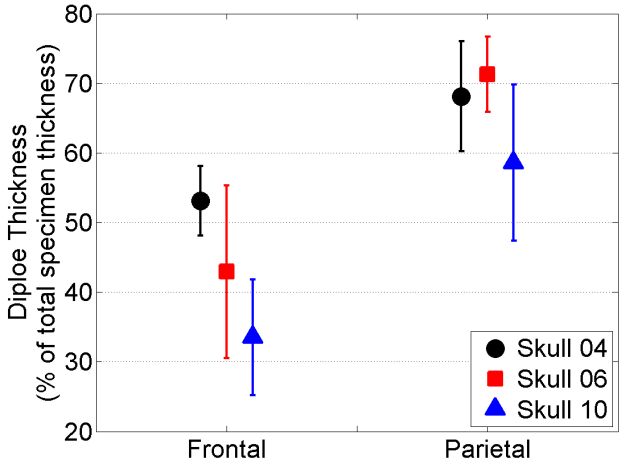

Fig. 11 Average values of the thickness percentage of the diploë, t_d

Table 6 Relative diploë thickness percentage, t_d

Grouping	mean ± std	Connecting symbols
Skull 06, parietal	71.3 ± 5.4	*
Skull 04, parietal	68.1 ± 7.9	* #
Skull 10, parietal	58.6 ± 11.2	# @
Skull 04, frontal	53.1 ± 5.0	@ &
Skull 06, frontal	42.9 ± 12.4	& §
Skull 10, frontal	33.5 ± 8.3	§
Skull 04, pooled	60.6 ± 10.0	¶
Skull 06, pooled	57.1 ± 17.3	¶
Skull 10, pooled	46.1 ± 16.1	◀
Parietal, pooled	66.0 ± 9.8	^
Frontal, pooled	43.2 ± 11.9	$

Note: Results are in units of thickness percentage (%). Groups that do not share the same symbol in the Connecting symbols column are significantly different.

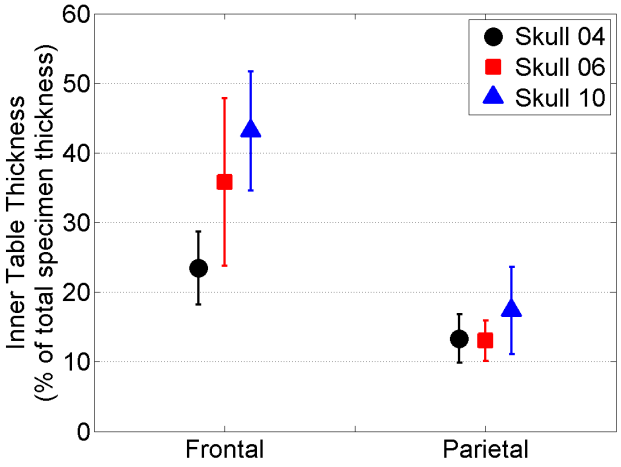

Fig. 12 Average values of the thickness percentage of the inner table, t_i

Table 7 Relative inner table thickness percentage, t_i

Grouping	mean ± std	Connecting symbols
Skull 10, frontal	43.1 ± 8.6	*
Skull 06, frontal	35.8 ± 12.0	*
Skull 04, frontal	23.5 ± 5.3	#
Skull 10, parietal	17.4 ± 6.3	# @
Skull 04, parietal	13.3 ± 3.5	@
Skull 06, parietal	13.0 ± 2.9	@
Skull 10, pooled	30.3 ± 15.1	¶
Skull 06, pooled	24.4 ± 14.5	◀
Skull 04, pooled	18.4 ± 6.8	Δ
Frontal, pooled	34.1 ± 12.0	^
Parietal, pooled	14.6 ± 4.7	$

Note: Results are in units of thickness percentage (%). Groups that do not share the same symbol in the Connecting symbols column are significantly different.

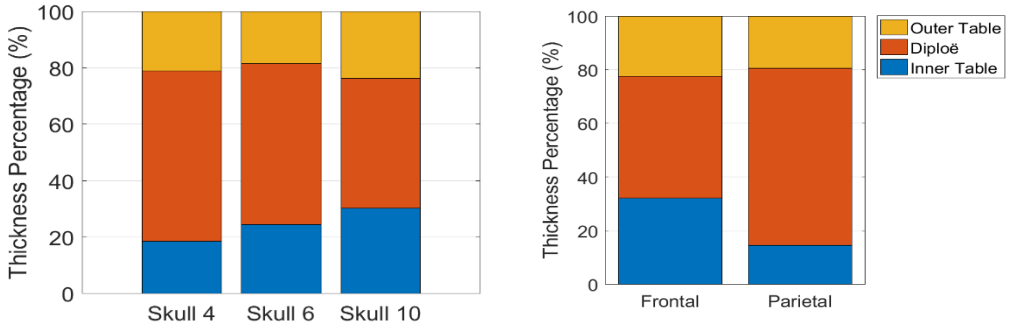

Fig. 13 Layer thickness percentages averaged over each skull (left) and bone type (right). Standard deviations are shown in Fig. 14.

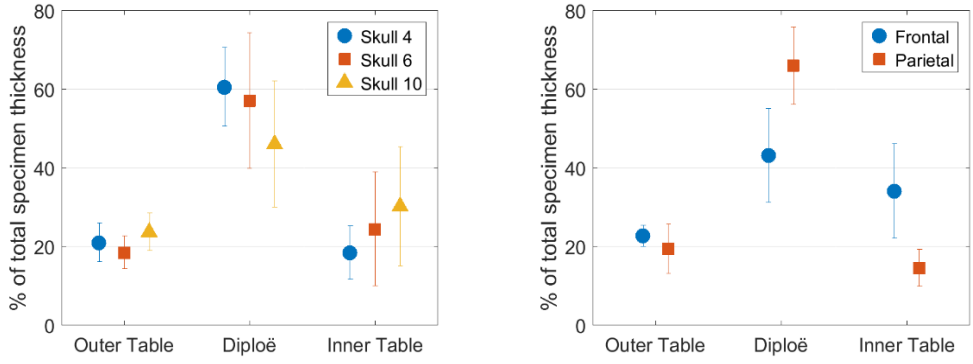

Fig. 14 Layer thickness percentages (shown in Fig. 13) with standard deviations. Absolute values in millimeters are shown in Appendix C, Figure C-1.

3.3 Porosity of Each Layer

The average porosity of each of the 3 layers was calculated from the change of porosity with depth, *P(d)*. The porosity profile was averaged along the depth corresponding to each of the layers. The method for identifying these layers was described in Section 3.2. The average porosity of each layer is reported in Tables 8–10. Figure 15 shows the layer porosities averaged by skull of origin (Skull 4, Skull 6, Skull 10) and by bone type (frontal, parietal). Figure 16 provides more detail, showing the average of each extraction grid.

Two-way ANOVA (Section 2.4) was conducted to determine the significance of the skull origin and bone type on the porosity of each layer. The results are listed in Table 11.

Table 8 Porosity percentage in the outer table

Grouping	mean ± std	Connecting symbols
Skull 04, parietal	12.6 ± 2.6	*
Skull 06, parietal	9.5 ± 3.5	#
Skull 04, frontal	6.9 ± 1.3	# @
Skull 10, parietal	6.7 ± 2.2	# @
Skull 06, frontal	5.3 ± 0.9	@
Skull 10, frontal	4.1 ± 0.6	@
Skull 04, pooled	9.7 ± 3.5	¶
Skull 06, pooled	7.4 ± 3.3	◄
Skull 10, pooled	5.4 ± 2.1	Δ
Parietal, pooled	9.6 ± 3.6	^
Frontal, pooled	5.4 ± 1.5	$

Note: Groups that do not share the same symbol in the Connecting symbols column are significantly different.

Table 9 Porosity percentage in the diploë

Grouping	mean ± std	Connecting symbols
Skull 10, Parietal	64.5 ± 10.4	*
Skull 04, Parietal	62.8 ± 2.4	*
Skull 04, Frontal	61.9 ± 2.2	*
Skull 06, Parietal	61.4 ± 1.3	*
Skull 10, Frontal	59.9 ± 6.2	*
Skull 06, Frontal	48.4 ± 3.9	#
Skull 04, pooled	62.3 ± 2.3	¶
Skull 10, pooled	62.2 ± 8.6	¶
Skull 06, pooled	54.9 ± 7.2	◀
Parietal, pooled	62.9 ± 6.1	^
Frontal, pooled	56.7 ± 7.4	$

Note: Groups that do not share the same symbol in the Connecting symbols column are significantly different.

Table 10 Porosity percentage in the inner table

Grouping	mean ± std	Connecting symbols
Skull 06, Parietal	20.0 ± 5.4	*
Skull 06, Frontal	19.8 ± 6.2	*
Skull 04, Frontal	19.1 ± 3.4	* #
Skull 04, Parietal	14.2 ± 2.6	* # @
Skull 10, Parietal	13.6 ± 3.8	# @
Skull 10, Frontal	12.1 ± 2.6	@
Skull 06, pooled	19.9 ± 5.6	¶
Skull 04, pooled	16.6 ± 3.9	¶
Skull 10, pooled	12.8 ± 3.2	◀
Frontal, pooled	17.0 ± 5.5	^
Parietal, pooled	15.9 ± 4.9	^

Note: Groups that do not share the same symbol in the Connecting symbols column are significantly different.

Table 11 Effects of bone type and skull origin on porosity percentage

Layer	Bone type	Skull of origin	Interaction
Outer table	X	X	. . .
Diploë	X	X	X
Inner table	. . .	X	. . .

Note: Factors that were significant in the 2-way ANOVA analysis ($p < 0.05$) are listed with an "X".

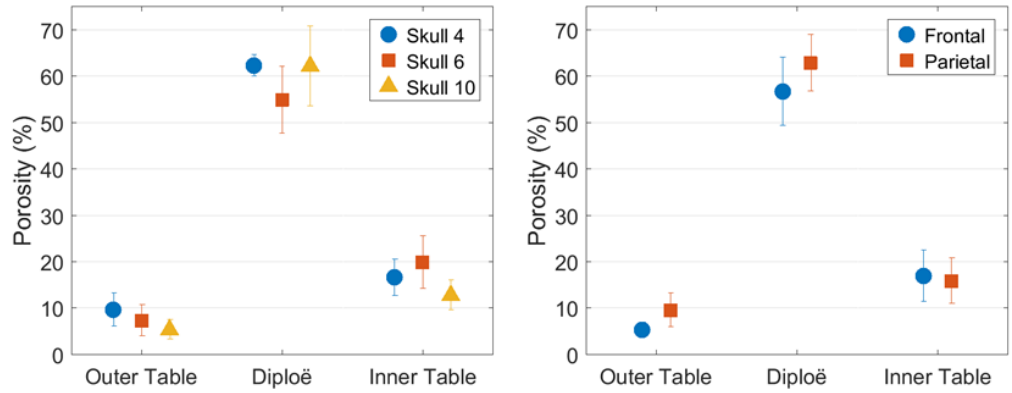

Fig. 15 Porosity of each layer, averaged by skull of origin (left) and by bone type (right)

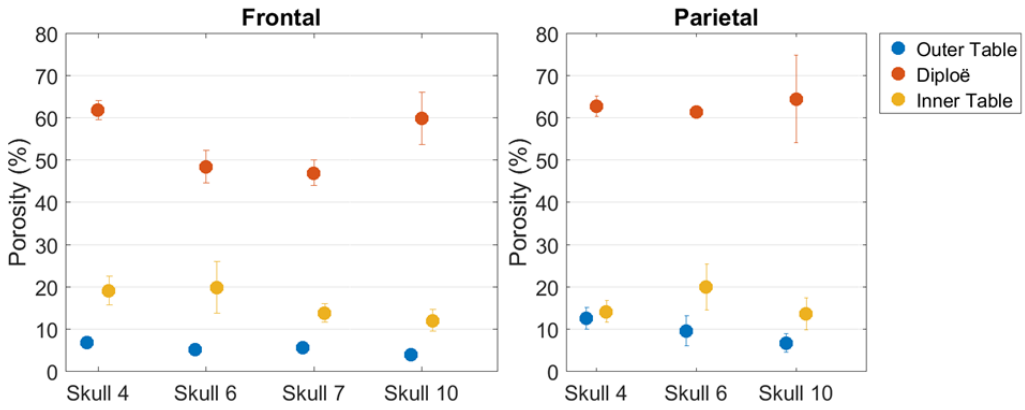

Fig. 16 Porosity of each layer, averaged by extraction grid

3.4 Fitting Gaussian Functions to the Measured Porosity-Depth Profiles

To further study the change of porosity with depth, a one-term Gaussian function was fitted and optimized to *P(d)*, as measured using micro-CT. The Gaussian function was given by

$$P^G(d) = Ae^{-[(d-B)/C]^2}. \quad (1)$$

Equation 1 was fit to the *P(d)* measurements for each specimen, using the fit function of MATLAB. Three parameters *A*, *B*, and *C* represented the Gaussian function as shown in Fig. 17. In Eq. 1, *A* describes the peak porosity reached in the diploë and will be referred to as the amplitude. The parameter *B* describes the depth, *d*, at which the porosity peaks. The parameter *C* is related to the spread of the porosity distribution along the depth, and is the percent width when the porosity is equal to $Ae^{-1/4}$, or roughly 78% of *A*.

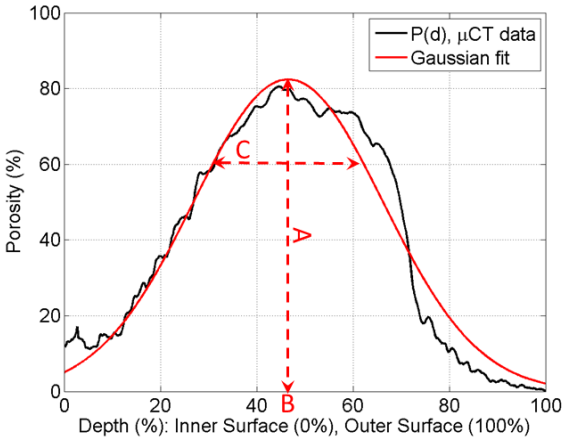

Fig. 17 Porosity profile of Specimen 04-03 (Fig. 7) with the Gaussian fit, $P^G(d)$. The 3 Gaussian parameters are shown schematically. For this example, results were A = 82%, B = 47%, C = 28%, and R^2 = 0.96.

The correlation coefficient, R^2, was also calculated for each Gaussian fit. Low correlation coefficients were observed for specimens exhibiting unusual phenomena, which could not be adequately modeled with a Gaussian function. R^2 = 0.65 was selected as the threshold and specimens with $R^2 < 0.65$ were not used in calculation of summary statistics. Three specimens fell into this category: 06-01, 06-04, and 06-07. These cases are presented in the discussion (Section 4.3).

The mean and standard deviation (std or σ) of the parameters A, B, and C were calculated for each of the statistical groups as described in Section 2.4. Figure 18 shows plots of the resulting Gaussian function with the mean ± σ.

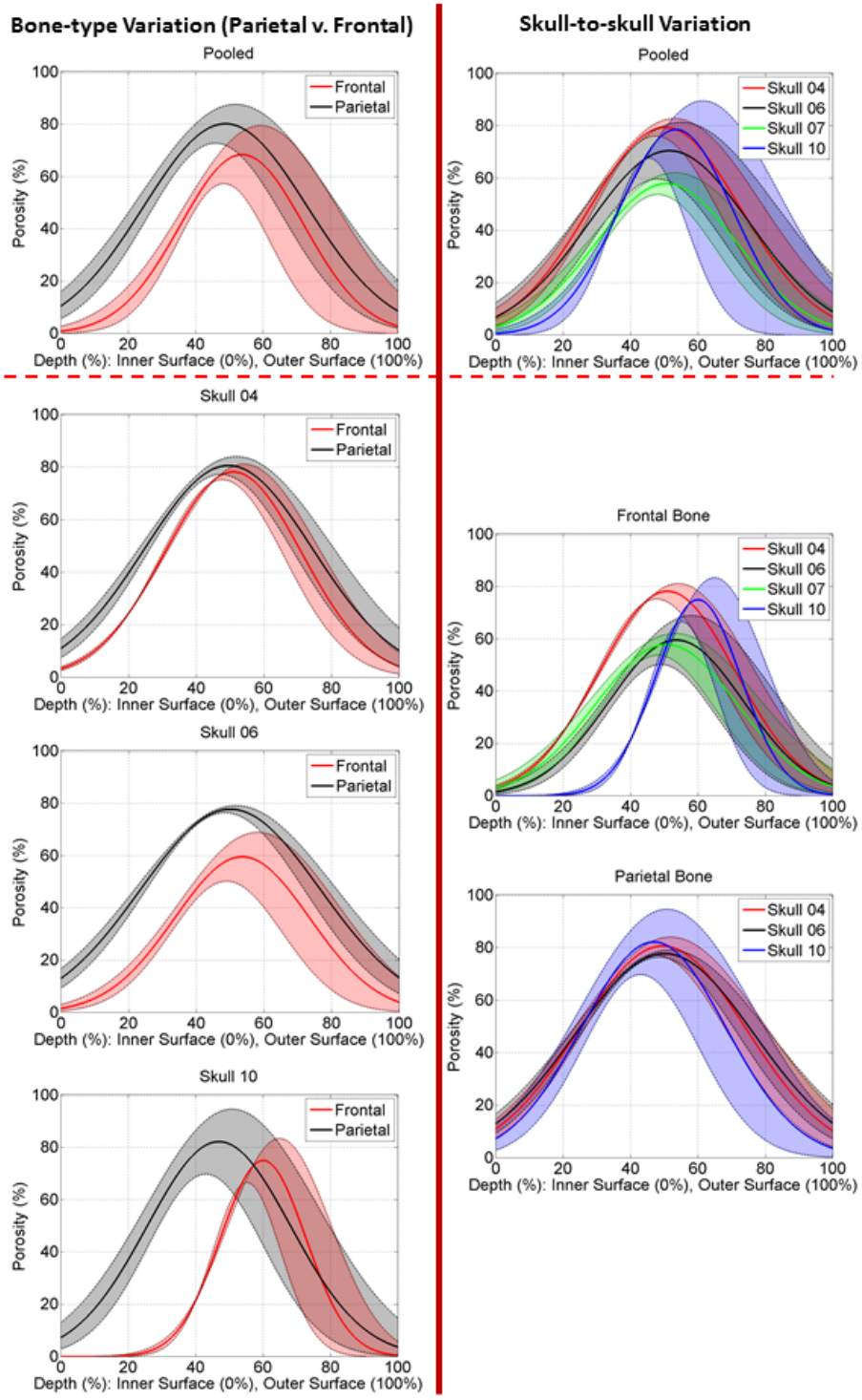

Fig. 18 Average Gaussian fits of the porosity profiles. The solid line shows the Gaussian function (Eq. 1) derived using the mean parameters. The shaded area represents corridors of ±σ of the Gaussian function.

Two-way ANOVA (Section 2.4) indicated that both skull origin and bone type were significant effects for all 3 parameters *A*, *B*, and *C* ($p < 0.05$). The interaction effect between these 2 sources of variation was only significant for parameters *A* and *B*.

Figures 19–21 show the mean and standard deviation for the parameters *A*, *B*, and *C*, respectively. These statistics are also reported in Tables 12–14, while also indicating which groups are statistically different. Appendix B contains box plots (based on quartiles) of the parameters *A, B,* and *C*.

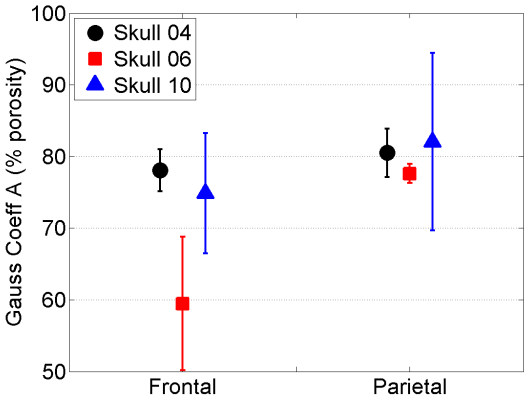

Fig. 19 Average values of the Gaussian coefficient *A*, related to the peak porosity (Fig. 17)

Table 12 Gaussian coefficient A

Grouping	mean ± std	Connecting symbols
Skull 10, parietal	82.1 ± 12.4	*
Skull 04, parietal	80.5 ± 3.4	*
Skull 04, frontal	78.1 ± 2.9	*
Skull 06, parietal	77.6 ± 1.3	*
Skull 10, frontal	74.9 ± 8.4	*
Skull 06, frontal	59.5 ± 9.3	#
Skull 04, pooled	79.3 ± 3.3	¶
Skull 10, pooled	78.5 ± 10.9	¶
Skull 06, pooled	70.4 ± 10.8	◀
Parietal, pooled	80.1 ± 7.4	^
Frontal, pooled	72.2 ± 10.2	$

Note: Results are in units of porosity percent (%). Groups that do not share the same symbol in the Connecting symbols column are significantly different.

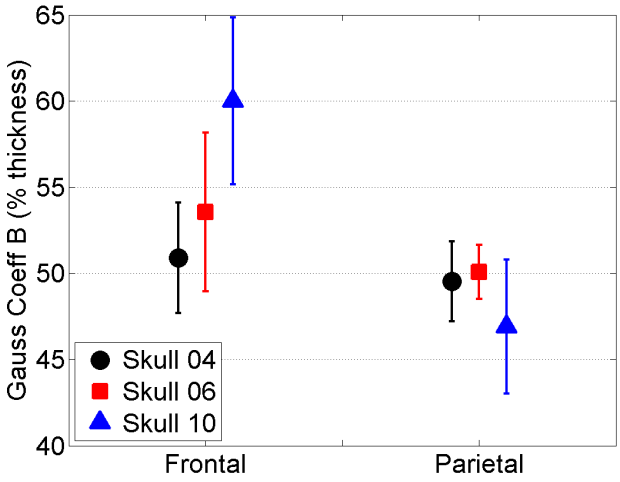

Fig. 20 Average values of the Gaussian coefficient *B*, which is the thickness percentage at which the porosity peaks (Fig. 17)

Table 13 Gaussian coefficient B

Grouping	mean ± std	Connecting symbols
Skull 10, frontal	60.0 ± 4.8	*
Skull 06, frontal	53.6 ± 4.6	#
Skull 04, frontal	50.9 ± 3.2	# @
Skull 06, parietal	50.1 ± 1.6	# @
Skull 04, parietal	49.5 ± 2.3	# @
Skull 10, parietal	46.9 ± 3.9	@
Skull 10, pooled	53.5 ± 8.0	¶
Skull 06, pooled	51.5 ± 3.5	¶ ◀
Skull 04, pooled	50.2 ± 2.8	◀
Frontal, pooled	55.0 ± 5.8	^
Parietal, pooled	48.8 ± 3.0	$

Note: Results are in units of thickness percentage (%). Groups that do not share the same symbol in the Connecting symbols column are significantly different.

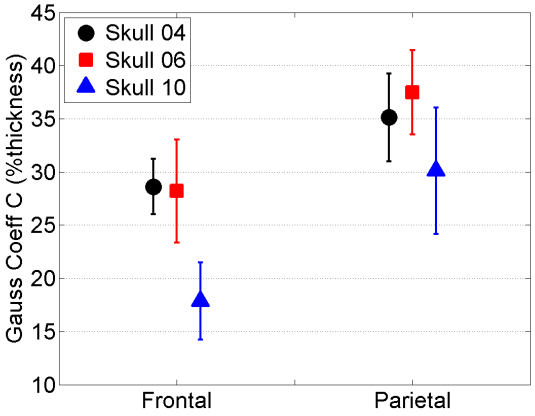

Fig. 21 Average values of the Gaussian coefficient *C*, related to the spread of the porosity distribution (Fig. 17)

Table 14 Gaussian coefficient C

Grouping	mean ± std	Connecting symbols
Skull 06, parietal	37.5 ± 4.0	*
Skull 04, parietal	35.1 ± 4.1	* #
Skull 10, parietal	30.1 ± 5.9	# @
Skull 04, frontal	28.6 ± 2.6	@
Skull 06, frontal	28.2 ± 4.8	@
Skull 10, frontal	17.9 ± 3.6	&
Skull 06, pooled	33.8 ± 6.3	¶
Skull 04, pooled	31.9 ± 4.7	¶
Skull 10, pooled	24.0 ± 7.9	◀
Parietal, pooled	34.2 ± 5.5	^
Frontal, pooled	24.5 ± 6.3	$

Note: Results are in units of thickness percentage (%). Groups that do not share the same symbol in the Connecting symbols column are significantly different.

3.5 Pore Orientation

Additional micro-CT scans were performed to visualize the much finer details of orientation of the porous structure in the outer table of 2 of the specimens. Specimens 10-02 and 04-12 were used to include results from both frontal bone (10-02) and parietal bone (04-12). Scanning parameters for these scans are listed in Table 15. These parameters were carefully selected to maximize resolution while minimizing image noise, with the result that scanning time for each specimen exceeded 50 h. After completion of the scan, the image stack was then rotated as previously described (Section 2.2). The VOI was created to only include the images of the outer table. The top-most image and the ROIs in the transverse planes were

selected using the same procedures as described in Section 2.2. The bottom of the VOI corresponded to the bottom-most image of the outer table. Selection of this bottom-most image was based on visual inspection, excluding images from the transition zone between the outer table and the diploë. To identify this bottom-most image, the operator started from the outer surface and traversed toward the diploë region. The first image that showed a marked increase in porosity was selected as the bottom of the VOI. The resulting thickness of the outer table for these procedures, t_0^*, was necessarily smaller than the thickness of the outer table as calculated by the method for layer identification previously presented (t_o, Section 3.2). The thickness of the outer tables selected by this method were t_0^* = 1.42 mm and t_0^* = 1.11 mm for Specimens 10-02 and 04-12, respectively.

Table 15 Scanning parameters for high-resolution, low-noise scans

Resolution/voxel size (µm)	Frame avg. (no. of frames)	Rotation step (°)	Random movement	Approx. scan time (h)
3.7	20	0.05	20	55.5

After VOI selection, the images were filtered (Gaussian, σ = 1) and then binarized so that the pores were displayed as white objects and the bone as black background. Thresholds were determined manually to satisfy the competing interests of preserving small porous features (increasing the threshold value) while avoiding image noise (decreasing the value). First, the threshold values corresponding to the automated binarization of several unfiltered images in the image stack were obtained using CTAn. This binarizing feature of CTAn is based on the unfiltered image and uses the Otsu method (Otsu 1975). However, in the current study, images were first filtered prior to final binarization. Therefore, threshold values were able to be used which were higher than those that were automatically generated by CTAn. Using higher values on the filtered image maximized the porous space that was preserved during binarization while still avoiding image noise. Starting with the automated values produced by CTAn, a trial-and-error method was used to increase the thresholds to the maximum possible value before image noise was seen in the resulting filtered-binarized image.

After binarization, CTVox (Bruker micro-CT) was used for 3-D visualization of the images. Figure 22 provides an overview of the process to visualize the arrangement of the pore structure in the outer table of Specimen 10-02. Figure 23 shows pores in the outer table of Specimen 04-12. The micro-CT software CTAn (Bruker micro-CT) was used to calculate the average thickness (diameter) of the pores within the outer table region of the 2 specimens. The average diameters were 90 and 86 µm for Specimens 10-02 and 04-12, respectively.

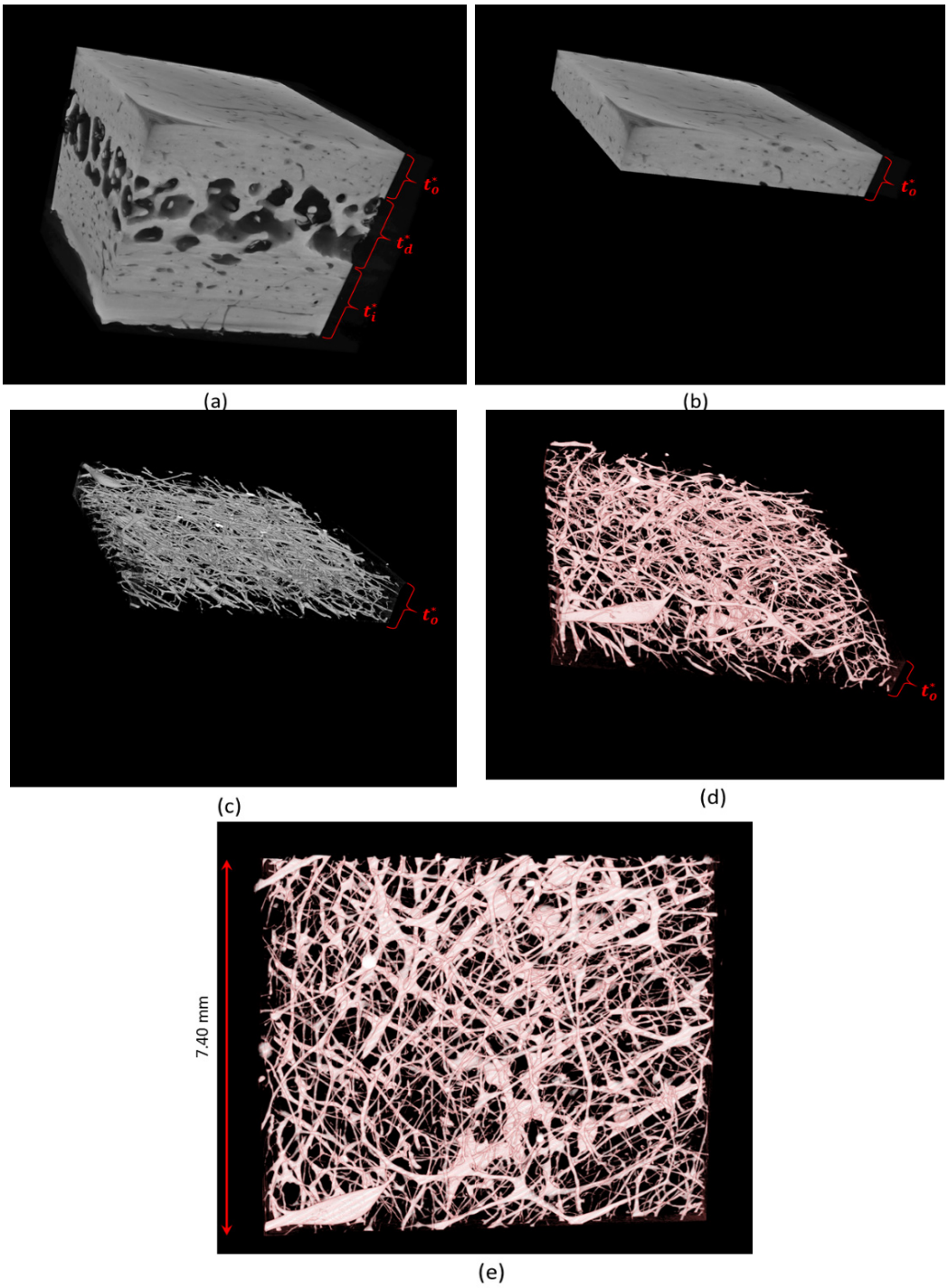

Fig. 22 Digitally coloring the pores in the outer table of Specimen 10-02 (from frontal bone). (a) The entire specimen. (b) The outer table selection, with thickness t_0^* = 1.42 mm. (c) The pores in the outer table. (d) The pores in the outer table, with digital color added. (e) A top-down view of the pores, looking down on the outer surface of the specimen. Average pore diameter = 90 µm.

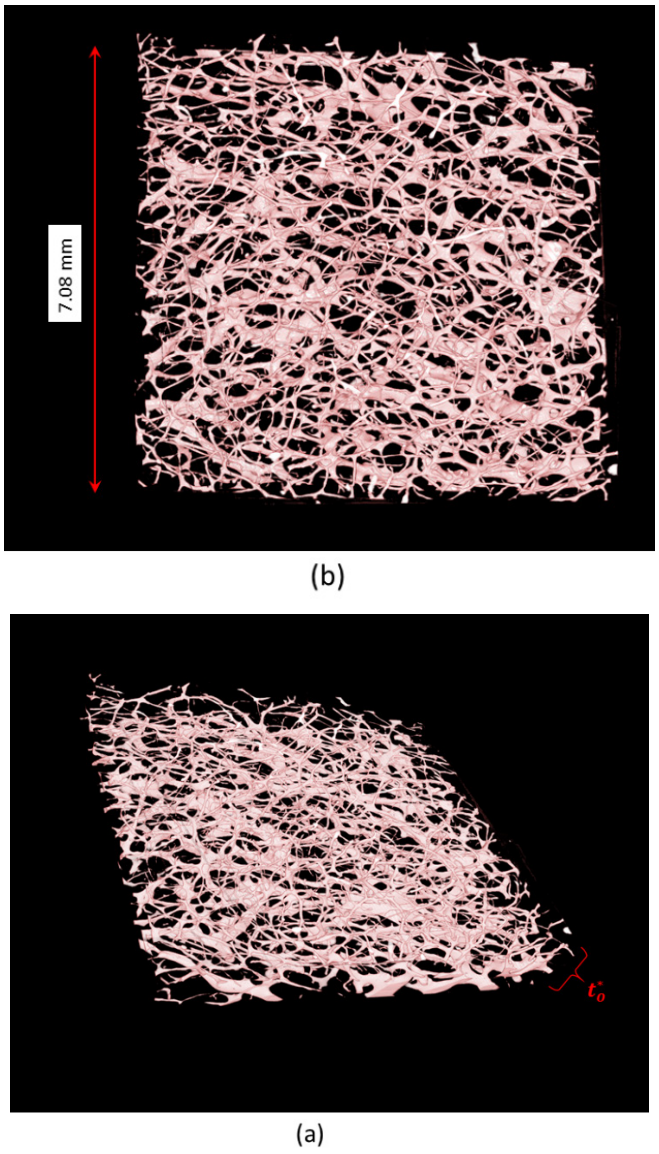

Fig. 23 Pores within the outer table of Specimen 04-12 (from parietal bone). The side view (a) and top-down view (b), are analogous to Fig. 22 (d) and (e). Outer table thickness, t_0^* = 1.11 mm. Average pore diameter = 86 µm.

4. Discussion

The change of porosity through the thickness of the skull measured in this report provided more insight than previous studies reported in literature. The method that was presented was analogous to examining serial sections separated by less than 10 µ and which were perpendicular to the normal at the center of the outer surface. This method provided the porosity variation in the skull at a much higher resolution, compared to previously reported porosities averaged over the entire thickness (Motherway et al. 2009; Rahmoun et al. 2014) or averaged over each of the 3 layers

(Boruah et al. 2013). The most striking feature of the high-resolution porosity profile was the peak porosity observed in the diploë (e.g., Fig. 7). This porosity peak has implications for the mechanical response of the skull because mechanical properties of porous bone have been reported to weaken with increasing porosity, to an exponential factor.

Porosity variation, *P(d)*, was described using a Gaussian function to systematically compare porosity profiles between samples. The 3 parameters that were calculated from the Gaussian fit (Eq. 1) defined the porosity of the diploë layer in the bone: the peak porosity of the diploë (*A*) in units of porosity percentage (%), the location of the peak porosity (*B*) in units of thickness percentage (%), and the relative spread in width (*C*) of the peak porosity in units of thickness percentage (%). Defining a standardized shape for the porosity profiles enabled interbone comparisons of the porosity distributions in the diploë, as measured by the peak (*A*) and width (*C*) of the Gaussian fit (discussed in the following paragraphs).

A method to objectively distinguish between the 3 layers of the skull based on *P(d)* was also presented in this report. Previously, layers were mostly identified using subjective methods, such as visualization with or without a microscope (e.g., McElhaney et al. 1970; Hubbard 1971; Peterson and Dechow 2002, 2003). Others have used digital images, without, however, specifying a systematic, repeatable approach (Ruan and Prasad 2001). The proposed method offered several possible improvements. First, the repeatability of layer identification was aided by relying on a quantitative threshold to distinguish the layers, based on the porosity. The only point of operator subjectivity was in the preliminary rotation of the image stack (discussed in Section 4.3.1). The few recent studies that used quantitative, rather than qualitative, methods to identify layers were not based on the change of porosity through the thickness (Boruah et al. 2013; Boruah et al. 2015; Lillie et al. 2015). Using the porosity variation for layer identification may provide a clearer link between morphology and mechanics due to the strong relationship that has been reported between the modulus and the porosity (Helgason et al. 2008).

Secondly, the present method, using a step size of less than 10 μ, was also based on much higher-resolution data compared to previous methods using only the unaided eye or an optical microscope (McElhaney et al. 1970; Hubbard 1971; Peterson and Dechow 2002, 2003). Finally, the present method also accounted for variations in the transverse plane. Observation of a bone segment using a light microscope only presents a surface view of the specimen. On the other hand, the porosity-depth profile underlying the present method was created by averaging across the sectional images of the specimen in the transverse plane. The limitations of the method are discussed in Section 4.3.3.

4.1 Frontal-Parietal Comparison in the Context of Skull-to-Skull Variability

The micrographs from frontal and parietal bones were clearly different by simple observation, even prior to resorting to quantitative analysis (e.g., Figs. 5 and 6). However, a large skull-to-skull difference was also visible at the same time. The analytical methods of this report helped to distinguish these 2 sources of variation. A total of 10 parameters were calculated for each specimen: 4 measures of relative layer thickness (as described in Section 3.2), the average porosity of each of the 3 layers (Section 3.3), and the 3 parameters of the Gaussian fit (Section 3.4). Two-way ANOVA indicated that both interbone and interskull effects were significant sources of variation for all parameters except for the porosity of the inner table.

However, further analysis indicated that the most pronounced differences between frontal and parietal bones may be in the relative thickness of the diploë and the inner table. Table 16 summarizes the results reported in Sections 3.2, 3.3, and 3.4, indicating which skulls had significant differences between their frontal and parietal bones in each of the 10 parameters.

Table 16 Skulls with significant differences between frontal and parietal bones

Parameter	Skulls	Bone type with greater mean value	Reference table
Overall thickness (t, mm)	Skull 4	Frontal	Table 4
Outer table thickness (t_o, %)	(none)	. . .	Table 5
Diploë thickness (t_d, %)	Skulls 4, 6, and 10	Parietal	Table 6
Inner table thickness (t_i, %)	Skulls 4, 6 and 10	Frontal	Table 7
Porosity of outer table	Skulls 4 and 6	Parietal	Table 8
Porosity of diploë	Skull 6	Parietal	Table 9
Porosity of inner table	(none)	. . .	Table 10
Peak porosity (A)	Skull 6	Parietal	Table 12
Depth of peak porosity (B)	Skull 10	Frontal	Table 13
Width of peak porosity (C)	Skulls 4, 6, and 10	Parietal	Table 14

Note: Summarized from the tables listed in the "Reference table" column.

Significant differences between the frontal and parietal bones in each of the 3 skulls was only seen for 3 parameters: t_d, t_i, and C. Both t_d and C are measures of the relative thickness of the diploë, and both were significantly higher in the parietal bones than in the frontal bones of the 3 skulls. This difference indicates that the parietal bones had a larger diploë region. The parameter t_i is the relative thickness of the inner table, and it was larger in the frontal bones than in the parietal bones. Taken together, the frontal-parietal differences of these 3 parameters indicate that the parietal bones have larger diploë layers than frontal bones, and that the parietal

bones compensate with correspondingly smaller inner tables. These differences were clearly visible in Figs. 13 and 14.

We are not aware of any other literature reporting this observed tradeoff in thickness between the diploë and the inner table. For example, Boruah et al. (2015) reported that the inner table was significantly larger in the parietal bone than in the frontal bone for 5 out of 10 tested skulls. However, the same report also found the outer table to be larger in the parietal bone than in the frontal bone for 5 out of 10 skulls; whereas, this difference in outer table thickness was not seen in the present study. The study of Boruah et al. (2015) also did not find the diploë to be consistently thicker in a particular bone type. The differences in results are likely due to different methods for layer identification (discussed below). Differences could also be due to the smaller number of samples in the current study, which used only 3 skulls to draw frontal-parietal comparisons.

The tradeoff seen in the parietal bone, between an increased diploë thickness and decreased inner table thickness, could also explain a primary point of divergence between the present results and previous reports. Many authors have reported that, on average, the outer table is thicker than the inner table (Hubbard 1971; Peterson and Dechow 2002; Boruah et al. 2013; 2015). However, the present study found this to only occur in extraction grids from the parietal bones and not from frontal bones (see Appendix C, Table C-1). This finding could be a result of the thinner inner table in parietal bones, which compensate for a thicker diploë.

In this study, the relative thickness of the outer table was not significantly different between the frontal and parietal bones. The lack of a consistent frontal-parietal difference in outer table thickness has also been reported in previous studies. (Peterson and Dechow 2003; Boruah et al. 2015)

The observations of the overall thickness (Table 4) showed that any difference in thickness between the frontal and parietal bones may be inconsistent and may be overruled by skull-to-skull variability. For example, in only 1 skull was the overall thickness significantly different between the 2 bone types. Moreover, the overall thicknesses of the frontal bones of each of the 3 skulls were significantly different (Table 4), and this was the only occurrence when a parameter was significantly different between each of the 3 skulls within a given bone type.

The difference in the peak porosity of the diploë, parameter A, between the 2 bone types may not be as pronounced or repeatable as the difference in relative diploë thickness. In only 1 of the 3 skulls was the parameter A significantly different between the frontal and parietal bones; whereas, the difference in diploë thickness percentage was significant for all 3 skulls. Boruah et al. (2015) also found

inconsistent trends between skulls when comparing the bone volume fraction (the complement of porosity) of the diploë between the frontal and parietal bones.

4.2 Porous Space in the Outer Table

The structure of load-bearing bones is highly anisotropic, with osteons aligned in the direction of physiological loading to reinforce the bone. However, the human skull is not generally considered a load-bearing bone. Therefore, preferential alignment of the osteons in the tables of the skull cannot be assumed a priori, and their arrangement has not been fully characterized or reported in literature.

We characterized the microstructure of the small pores in the outer table using high-resolution micro-CT to observe if the pores were preferentially aligned along a given direction. The pores within the tables included the Haversian canals, which are the central cylindrical pores of osteons. Therefore, the alignment of the pores provides an indication of osteonal alignment, implying the degree of structural and mechanical anisotropy.

The long axis of the porous canals were generally oriented in the transverse plane, and no predominant orientation within this plane was visible in the high-resolution micro-CT scans of the upper table of the skull (Figs. 22 and 23). These figures originated from 2 different bone types (frontal and parietal) from 2 different skulls (04 and 10). They provide high-resolution confirmation of the observation reported by McElhaney et al. (1970), which was based on observation of serial sections of cranial bone using unspecified methods.

The random arrangement in the transverse plane is in sharp contrast to the preferential alignment of osteons along the loading direction in load-bearing bones such as the femur. As a means of comparison, Fig. 24 provides a 3-D representation of the porous space within the outer cortical region of a human femur specimen used by our group as part of a different set of experiments (Sanborn et al. 2016).

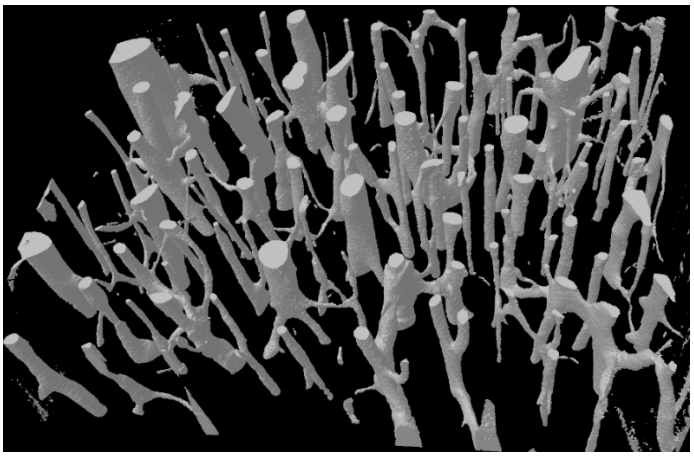

Fig. 24 Porous space within the outer cortical region of a human femoral bone specimen, visualized with micro-CT. The pores are shown as grey objects.

4.3 Assumptions, Limitations, and Sources of Error Associated with Quantitative Porosity Assessment

The goal of the quantitative analysis of skull structure was to maximize the repeatability of measurements to draw comparisons between extraction grids, bone types, and skulls. Nevertheless, several factors may introduce error into these comparisons.

Error could have arisen in the comparison of bone types (frontal, parietal) across different skulls. These comparisons implicitly assumed that the extracted specimens were comparable across skulls. Care was taken to extract bone sections from the skull that appeared similar in external features. However, variations were inevitable due to the variability associated with human skulls. An example is provided by the 3 specimens with failed Gaussian fits. In addition, each extraction grid of specimens was from a different distance away from the sutures (Table 1). The variability in distance from the sutures could introduce an additional variable if cranial structure changes as a function of these distances, which has been previously observed (McElhaney et al. 1970).

4.3.1 Measurement Error: Scanning Parameters and Image Postprocessing

Scanning parameter variations and subsequent postprocessing of the images could have introduced error into the porosity analysis. Four different sets of scanning parameters were used (Table 2) due to external circumstances. In addition, several postprocessing steps were necessary to calculate the porosity profile from the images. First, the outer surface of the specimen was rotated so that the surface normal at the center of the outer table was aligned in the vertical direction (Fig. 3).

However, this realignment could have introduced subjectivity due to the irregularity of the outer surface. After rotation, the pixels corresponding to the specimen, or ROI, were then separated from pixels representing the surrounding media on the top and the bottom of the specimen. Any uncertainty associated with the ROI selection could have a direct impact on the measurement of overall thickness, *t*, considering it is calculated from the overall height of the image stack. Finally, the images were converted from gray scale to a binary format for the quantitative image analysis. An automated algorithm was used to eliminate operator subjectivity in the threshold identification for the grayscale images.

Appendix A presents a quantification of measurement error arising from scanning parameter differences and postprocessing procedures. Specimen 06-25 was scanned under different parameters, and the resulting images from each scan were also independently postprocessed. The variation between results indicated the total error associated with scanning parameter variation, image stack rotation, and specimen ROI selection. It was concluded that the total measurement error for each parameter was much lower than the amount of specimen-to-specimen deviation within an extraction grid, generally accounting for less than 10% of the total interspecimen variability.

4.3.2 Approximating the Porosity Variation with a Gaussian Function

In this study, the porosity-depth profile was assumed to be adequately described by a Gaussian distribution. The porosity-depth profiles of 60 from a total of 63 specimens were well described by the Gaussian function ($R^2 > 0.65$). The Gaussian curve was considered an inappropriate fit for only 3 specimens: 06-01, 06-04, and 06-07. These specimens did not have distinguishable inner tables with dense cortical bone. Instead, the region normally composed of the dense inner table was filled with large pores, creating a second porous region in addition to the diploë. As an example, Fig. 25 shows a through-thickness image of one of these specimens, 06-07. The in-situ arrangement of these 3 specimens was roughly along a vertical, superior-inferior line on the frontal bone (Fig. 2). Therefore, these porous regions in the inner table could be evidence of a persistent network of cavities oriented in the superior-inferior direction and near the inner surface. The skull contains veins in the diploë, and the inner surface had several foramina that allowed for passage of vessels into the cranial bone. The cavities near the inner surface of the specimens with low R^2 values were likely components of the vesicular passages from the meninges into the cranium. Indeed, various deviations from the canonical 3-layered morphology have also been reported elsewhere, accompanied by an inability to discretize the thickness into 3 separate layers (Ruan and Prasad 2001).

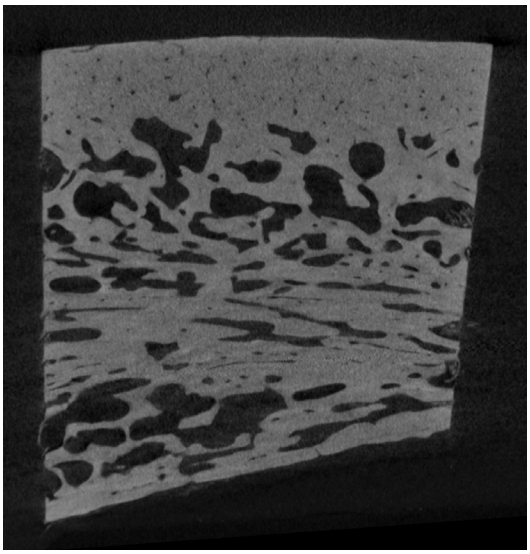

Fig. 25 Through-thickness image of Specimen 06-07. For this specimen, the porosity-depth profile could not be described by the Gaussian fit. A secondary porous region, in addition to the diploë, is evident near the inner surface (bottom of the figure).

4.3.3 Method for Layer Identification

A new, more repeatable method to distinguish between the layers was identified using the porosity-depth profile together with a cutoff percentage. This procedure was based on several assumptions. First, the outer and inner tables were assumed to consist entirely of cortical bone with a porosity less than 30%, and the diploë was assumed to be only trabecular bone with a porosity of greater than 30%. However, the porosity-depth profiles indicated a porosity gradient, and identification of a single cutoff value remained somewhat arbitrary. Moreover, the results indicated that the threshold of 30% may have been high, leading to inflated values for table thicknesses. For example, the inner table of many specimens, as identified by the present method, included regions where the porosity spiked above 30%. This could indicate that a lower threshold may be used in the future.

Secondly, the method assumed that the porosity only varied in the depth dimension, from the outer to inner surfaces, and that the porosity was constant in the transverse dimension. This assumption appeared to be valid based on the visual inspection of the micro-CT images (e.g., Fig. 5), and is further analyzed in Appendix D.

5. Conclusions

The change in porosity was measured across the thickness of the skull, from the outer to inner surfaces, using micro-CT with a resolution of less than 10 μ. The resulting porosity-depth profiles were used to calculate the thicknesses of the 3 layers of the skull: the outer and inner tables and the diploë. Each of the porosity-depth profiles were fit to a Gaussian function, from which the peak diploë porosity was calculated together with the spread of porosity across the depth. The measured parameters enabled a comparison between frontal and parietal bones while accounting for skull-to-skull variation, allowing us to reach the following conclusions:

- The diploë occupies relatively more thickness in the parietal bone than in the frontal bone. The increased thickness percentage of the diploë in the parietal bone appears to be compensated by a relatively thinner inner table. Given the porosity-modulus relationship, these differences would suggest that parietal bone is weaker than frontal bone.
- On the other hand, measurements of the total specimen thickness did not consistently show significant differences between the frontal and parietal bone. At the same time, there were significant differences between donors. For example, the thicknesses of frontal bone specimens were significantly different between all 3 skulls.
- The peak porosity reached in the diploë was not consistently different between the frontal and parietal bones.

Finally, the porous space within the outer tables of the frontal and parietal bones was imaged with micro-CT using a resolution less than 5 μm. The microstructural subunits of the outer table of the skull bone appeared randomly oriented in the transverse plane.

6. References

Alexander SL, Gunnarsson CA, Weerasooriya T. Structural influence on the mechanical response of adolescent Göttingen porcine cranial bone. Aberdeen Proving Ground (MD): Army Research Laboratory (US); 2016 Oct. Report No.: ARL-TR-7845.

Boruah S, Henderson K, Subit D, Salzar R, Shender B, Paskoff G. Response of human skull bone to dynamic compressive loading. In: Proceedings of the International Research Council on Biomechanics of Injury (IRCOBI) Conference; 2013 Sep 11–13; Gothenburg, Sweden: IRCOBI Vol. 13. p. 497.

Boruah S, Paskoff GR, Shender BS, Subit DL, Salzar RS, Crandall JR. Variation of bone layer thicknesses and trabecular volume fraction in the adult male human calvarium. Bone. 2015;(77):120–134.

Carter DR, Hayes WC. The compressive behavior of bone as a two-phase porous structure. The J of Bone and Joint Surgery. 1977;59(7):954–962.

Fry, FJ, Barger, JE. Acoustical properties of the human skull. The J of the Acoustical Soc of America. 1978;(63):1576–1590.

Goulet RW, Goldstein SA, Ciarelli MJ, Kuhn JL, Brown MB, Feldkamp LA. The relationship between the structural and orthogonal compressive properties of trabecular bone. J of Biomechanics. 1994;27(4):375–389.

Helgason B, Perilli E, Schileo E, Taddei F, Brynjólfsson S, Viceconti M. Mathematical relationships between bone density and mechanical properties: a literature review. Clinical Biomechanics. 2008;23(2):135–146.

Huang AH, Sun HH, Skolnick GB, Woo AS. Thickness of calvarium and diploic space in children ages 0 to 17 as assessed by computed tomography. European J of Plastic Surgery. 2015;38(3):193–198.

Hubbard RP. Flexure of layered cranial bone. J of Biomechanics. 1971;4(4): 251–263.

Lillie EM, Urban JE, Weaver AA, Powers AK, Stitzel JD. Estimation of skull table thickness with clinical CT and validation with micro-CT. J of Anatomy. 2015;226(1):73–80.

Lillie EM, Urban JE, Lynch SK, Weaver AA, Stitzel JD. Evaluation of skull cortical thickness changes with age and sex from computed tomography scans. J of Bone and Mineral Research. 2016;31(2):299–307.

Lynnerup N, Astrup JG, Sejrsen B. Thickness of the human cranial diploë in relation to age, sex and general body build. Head and Face Medicine. 2005;1(13):1–7.

McElhaney JH, Fogle JL, Melvin JW, Haynes RR, Roberts VL, Alem NM. Mechanical properties of cranial bone. J of Biomechanics. 1970;3(5):495–511.

Motherway JA, Verschueren P, Van der Perre G, Vander Sloten J, Gilchrist MD. The mechanical properties of cranial bone: the effect of loading rate and cranial sampling position. J of Biomechanics. 2009;42(13):2129–2135.

Mow VC, Huiskes R. Basic orthopaedic biomechanics and mechano-biology. Alphen aan den Rijn (Netherlands): Lippincott Williams and Wilkins; 2005.

Otsu, Nobuyuki. A threshold selection method from gray-level histograms. Automatica. 1975;11.285(296):23–27.

Peterson J, Dechow PC. Material properties of the inner and outer cortical tables of the human parietal bone. The Anatomical Record. 2002;268(1):7–15.

Peterson J, Dechow PC Material properties of the human cranial vault and zygoma. The Anatomical Record Part A: Discoveries in Molecular, Cellular, and Evolutionary Biology. 2003;274(1):785–797.

Peyrin F, Salome M, Nuzzo S, Cloetens P, Laval-Jeantet AM, Baruchel J. Perspectives in three-dimensional analysis of bone samples using synchrotron radiation microtomography. Cell Mol Biol. 2000; 46:1089–1102. Cited in: Cooper DML, Turinsky AL, Sensen CW, Hallgrimsson B. Quantitative 3D analysis of the canal network in cortical bone by micro-computed tomography. The Anatomical Record Part B: The New Anatomist. 2003.274(1):169–179.

Rahmoun J, Auperrin A, Delille R, Naceur H, Drazetic P. Characterization and micromechanical modeling of the human cranial bone elastic properties. Mech Research Comm. 2014;60:7–14.

Ruan J, Prasad P. The effects of skull thickness variations on human head dynamic impact responses. Stapp Car Crash J. 2001;45:395–414.

Sabanciogullari V, Salk I, Cimen M. The relationship between total calvarial thickness and diploë in the elderly. International J of Morphology. 2013;31(1):38–44.

Sanborn B, Gunnarsson CA, Foster M, Weerasooriya T. Quantitative visualization of human cortical bone mechanical response: studies on the anisotropic compressive response and fracture behavior as a function of loading rate. Experimental Mechanics. 2016;56(1)81–95.

Trammell LH. Neurocranial histomorphometrics [dissertation]. [Knoxville (TN)]: University of Tennessee; 2012.

INTENTIONALLY LEFT BLANK.

Appendix A. Analysis of Error Associated with Scanning Parameters and Postprocessing Steps

Specimen 06-25 was scanned 4 different times using the parameters described below in Table A-1. These scans were taken for the purpose of protocol determination and were not explicitly executed for error analysis. Nevertheless, the quantitative results can provide insight into the total error arising from the variation of scanning parameters used in the report (Table 2) and from the error involved in postprocessing. For example, the resolution of these scans ranged from 6.7 to 5.3 μm, which covered the full range of resolutions used in the report.

Table A-1 Micro-CT scanning parameters for error analysis

Scan no.	Resolution/voxel size (μm)	Frame avg. (no. of frames)	Rotation step (°)	Random movement	Filter
Scan 1	6.7	10	0.2	20	Al, 0.5 mm
Scan 2	6.1	10	0.2	20	none
Scan 3	6.1	10	0.2	20	Al, 0.5 mm
Scan 4	5.3	10	0.15	20	Al, 0.5 mm

Each dataset from each scan was postprocessed independently. The same methods as described in the report were used after each scan for image stack rotation, region of interest (ROI) selection, image binarization, the calculation of the porosity-depth profile *P(d)*, and the calculation of the Gaussian fit (Eq. 1). Similarly, the 4 parameters calculated in Section 3.2 from the porosity-depth profile (t, t_o, t_d, t_i) and the 3 parameters calculated in Section 3.4 from the Gaussian fit (A, B, and C) were also calculated for these scans. Figure A-1 shows the porosity-depth profiles from each scan and the Gaussian fits. Table A-2 reports the results for each of the 7 parameters.

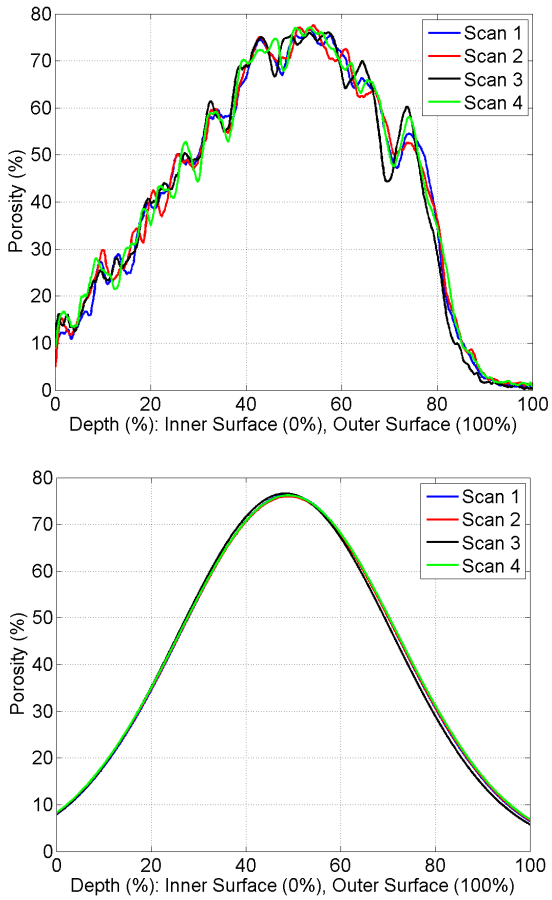

Fig. A-1 Porosity-depth profile from each scan (top) and the Gaussian fits (bottom)

Table A-2 Parameter results

Scan no.	t (μm)	t_o (%)	t_d (%)	t_i (%)	A (porosity %)	B (%)	C (%)
Scan 1	8122	19.4	63.8	16.8	76.3	49.0	32.5
Scan 2	8161	19.1	65.2	15.7	76.0	48.9	32.7
Scan 3	8259	20.2	63.0	16.8	76.6	48.4	32.1
Scan 4	8118	18.9	66.3	14.8	76.2	49.0	32.8
σ_M	65.5	0.6	1.5	0.9	0.3	0.3	0.3

Note: Units are in depth percentage points, except for parameters t and A, which are in units of μm and percent porosity, respectively. Also shown is the standard deviation due to measurement (σ_M) for each parameter.

The Coefficient of Reliability, R, has been used by others to relate the amount of variation due to measurement error to the total amount of inter-specimen variation.[1] Adapted to the present case, the Coefficient of Reliability for a given parameter can be defined by Eq. A-1:

[1] Ulijaszek SJ, Kerr DA. Anthropometric measurement error and the assessment of nutritional status. British J of Nutrition. 1999;82(03):165–177.

$$R = 1 - \frac{(\sigma_M)^2}{(\sigma_o)^2} \ . \qquad \text{(A-1)}$$

In Eq. A-1, the standard deviation due to measurement of the parameter is given by σ_M and the total, interspecimen standard deviation observed in the results is given by σ_o. The results for R are shown in Table A-3. R was calculated for each parameter using the σ_M from the error study of Spec 06-25 (Table A-2) together with the standard deviation values reported from each extraction grid (Sections 3.2 and 3.4).

Table A-3 Coefficient of Reliability (R) for each parameter

Extraction grid	t	t_o	t_d	t_i	A	B	C
Skull 4, frontal	98.2	96.9	91.4	96.8	99.3	99.1	98.4
Skull 4, parietal	95.8	98.8	96.6	92.6	99.4	98.2	99.4
Skull 6, frontal	99.7	87.4	98.6	99.4	99.9	99.5	99.5
Skull 6, parietal	98.5	98.1	92.7	89.3	96.5	96.1	99.3
Skull 10, frontal	99.3	95.0	96.9	98.8	99.9	99.6	99.2
Skull 10, parietal	99.1	99.2	98.3	97.7	100.0	99.4	99.7
Mean	98.4	95.9	95.8	95.8	99.2	98.6	99.2

Note: R is calculated for each parameter using Eq. A-1, and is reported in percentage (%).

The Coefficient of Reliability quantifies the amount of the variation observed in each extraction grid that was not due to measurement error.[2,3] In Table A-3, R was reported as greater than 90%, with only 2 exceptions. This indicates that measurement error associated with scanning parameter variation and postprocessing is generally accountable for less than 10% of the total amount of observed variation in each grid. Furthermore, even the lowest R value (87.4%) indicated that the total measurement error accounted for less than 13% of the interspecimen error.

[2] Ulijaszek SJ, Kerr DA. Anthropometric measurement error and the assessment of nutritional status. British Journal of Nutrition. 1999;82(03):165–177.

[3] Lewis SJ. Quantifying measurement error. In: S. Anderson, editor. Current and recent research in osteoarchaeology 2: 1999; Proceedings of the 4th, 5th and 6th meetings of the Osteoarchaeological Research Group. Barnsley (England): Oxbow Books. c1999. p. 54–55.

Appendix B. Box Plots of Results for the Gaussian Coefficients (*A, B,* and *C*)

Figures B-1 through B-3 present box plots of the results for the Gaussian coefficients *A*, *B*, and *C*, respectively. The box plots show the median, first and third quartiles, and whiskers extending to 1.5 times the interquartile range. Red dots indicate outliers beyond the extent of the whiskers. Each figure shows the bone-to-bone variation as well as the skull-to-skull variation. The mean and standard deviation of the results were presented in Tables 12–14 in the main report.

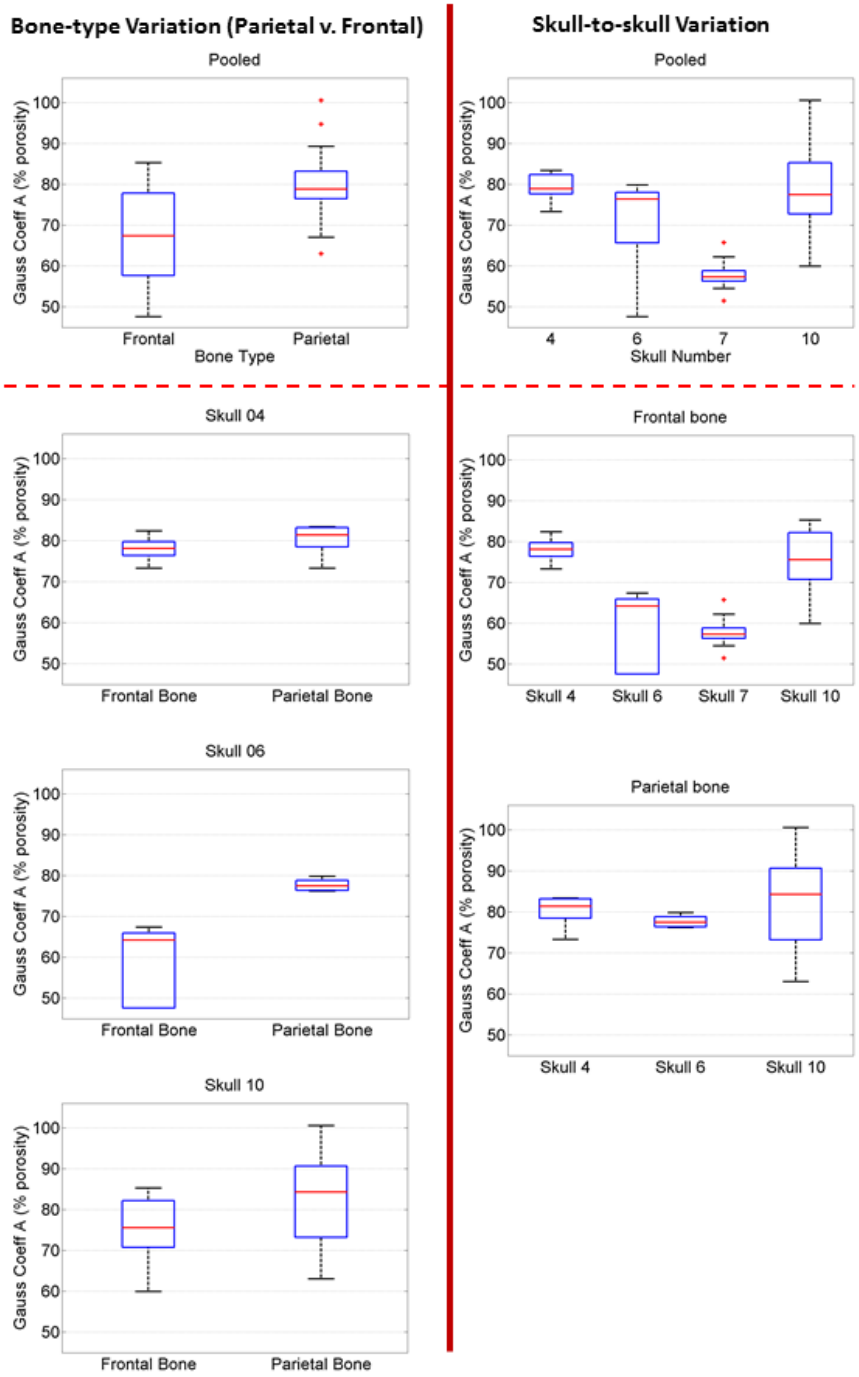

Fig. B-1 Box plots of the Gaussian coefficient *A*

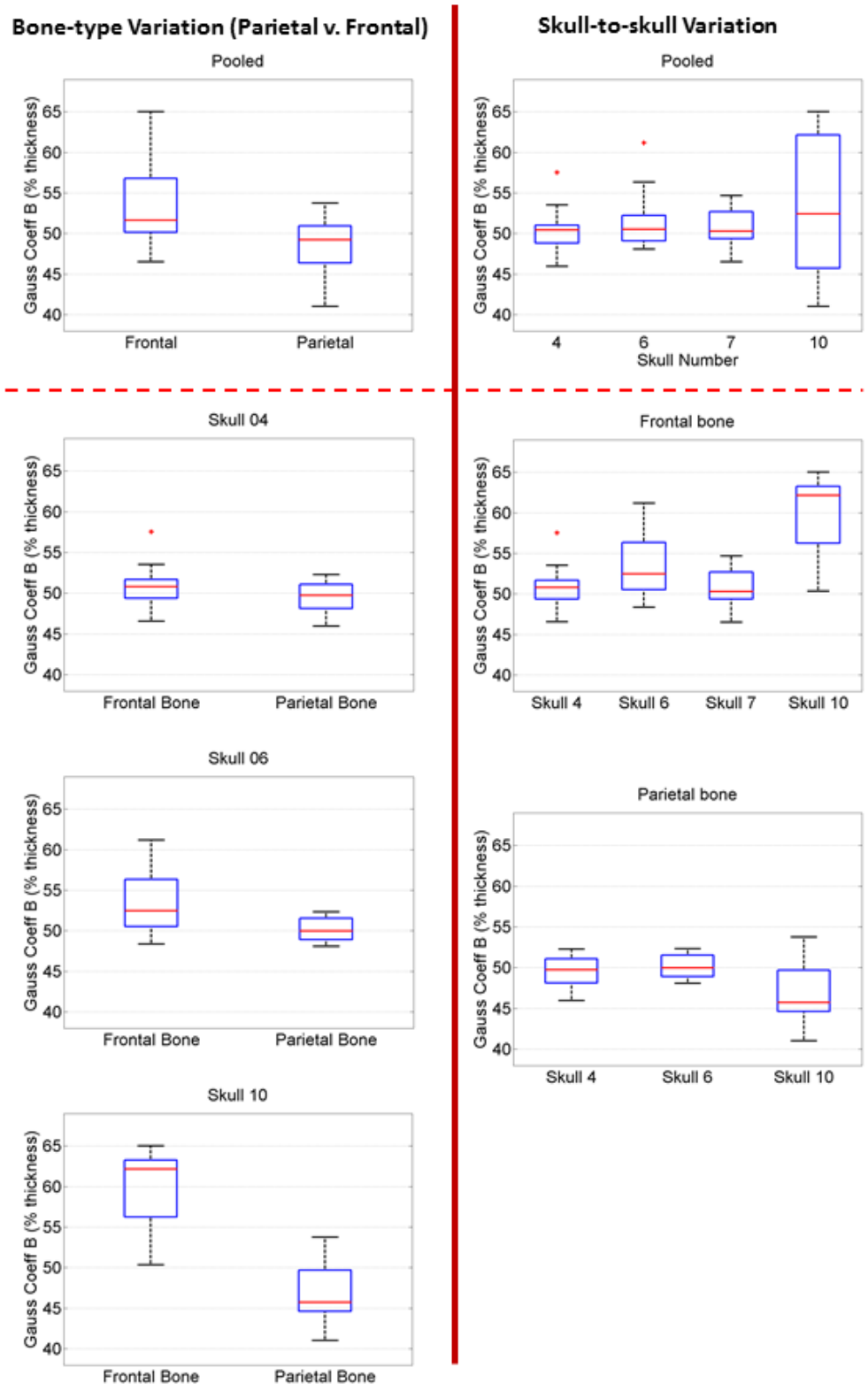

Fig. B-2 Box plots of the Gaussian coefficient *B*

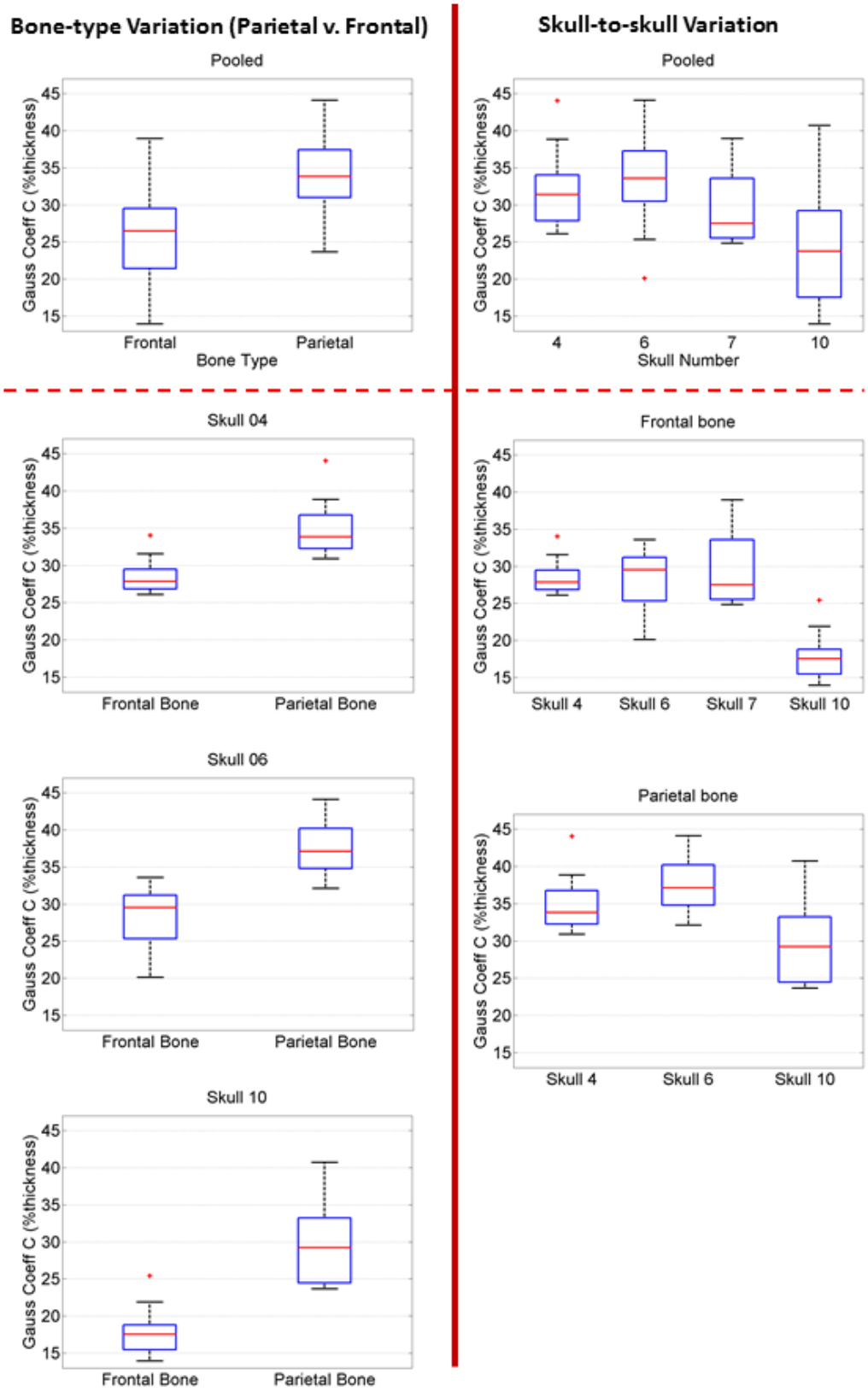

Fig. B-3 Box plots of the Gaussian coefficient *C*

Appendix C. Summary Data for the Thickness Parameters

Table C-1 lists the mean and standard deviation for the thickness percentages of the outer table (t_o), diploë (t_d), and inner table (t_i), as they were reported in Section 3.2 (Tables 5–7) of the main report. Table C-2 lists the absolute values (in millimeters) of the layer thicknesses, together with the total skull thickness (t). These are also shown in Fig. C-1. Figures C-2 through C-5 present box plots of the results for total skull thickness (t), as well as for t_o, t_d , and t_i. Each figure shows the bone-to-bone variation as well as the skull-to-skull variation.

Table C-1 Relative layer thicknesses (% of total thickness)

Grouping	t_o	t_d	t_i
Skull 04, frontal	23.5 ± 3.2	53.1 ± 5.0	23.5 ± 5.3
Skull 04, parietal	18.6 ± 5.3	68.1 ± 7.9	13.3 ± 3.5
Skull 06, frontal	21.2 ± 1.6	42.9 ± 12.4	35.8 ± 12.0
Skull 06, parietal	15.7 ± 4.2	71.3 ± 5.4	13.0 ± 2.9
Skull 07, frontal	21.7 ± 3.0	52.6 ± 11.1	25.7 ± 8.9
Skull 10, frontal	23.3 ± 2.6	33.5 ± 8.3	43.1 ± 8.6
Skull 10, parietal	24.1 ± 6.4	58.6 ± 11.2	17.4 ± 6.3
Skull 04, pooled	21.0 ± 5.0	60.6 ± 10.0	18.4 ± 6.8
Skull 06, pooled	18.5 ± 4.2	57.1 ± 17.3	24.4 ± 14.5
Skull 10, pooled	23.7 ± 4.8	46.1 ± 16.1	30.3 ± 15.1
Frontal, pooled	22.4 ± 2.7	45.5 ± 12.3	32.0 ± 11.8
Parietal, pooled	19.4 ± 6.3	66.0 ± 9.8	14.6 ± 4.7

Note: Summarized from Tables 5–7 of the main report.

Table C-2 Absolute layer thicknesses (mm)

Grouping	t	t_o	t_d	t_i
Skull 04, frontal	9.6 ± 0.5	2.3 ± 0.3	5.1 ± 0.5	2.3 ± 0.6
Skull 04, parietal	5.5 ± 0.3	1.0 ± 0.3	3.8 ± 0.3	0.7 ± 0.2
Skull 06, frontal	8.5 ± 1.1	1.8 ± 0.1	3.7 ± 1.4	3.0 ± 0.9
Skull 06, parietal	8.3 ± 0.5	1.3 ± 0.3	5.9 ± 0.7	1.1 ± 0.2
Skull 07, frontal	6.5 ± 0.6	1.4 ± 0.2	3.5 ± 0.9	1.7 ± 0.6
Skull 10, frontal	7.0 ± 0.8	1.6 ± 0.9	2.4 ± 0.7	3.0 ± 0.7
Skull 10, parietal	6.1 ± 0.7	1.5 ± 0.4	3.6 ± 0.9	1.0 ± 0.3
Skull 04, pooled	7.6 ± 2.1	1.6 ± 0.7	4.4 ± 0.8	1.5 ± 0.9
Skull 06, pooled	8.4 ± 0.9	1.5 ± 0.4	4.8 ± 1.6	2.1 ± 1.2
Skull 10, pooled	6.6 ± 0.8	1.5 ± 0.3	3.0 ± 1.0	2.0 ± 1.1
Frontal, pooled	7.9 ± 1.5	1.8 ± 0.4	3.7 ± 1.3	2.5 ± 0.9
Parietal, pooled	6.7 ± 1.3	1.3 ± 0.4	4.4 ± 1.3	1.0 ± 0.3

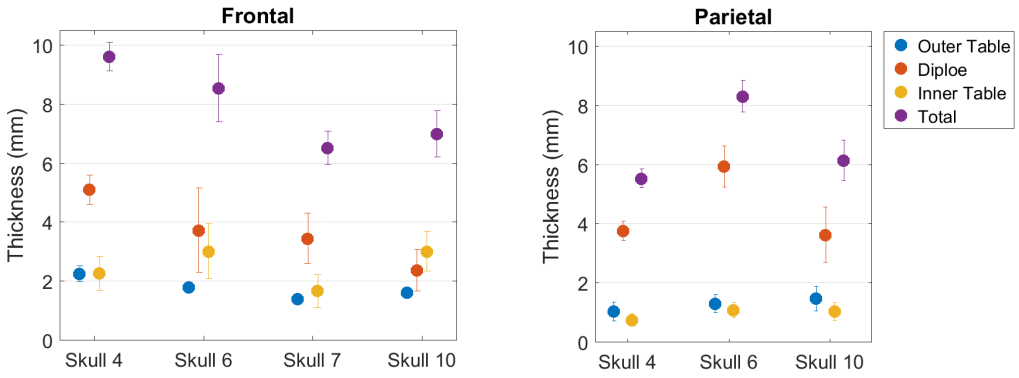

Fig. C-1 Absolute thickness measurements (mm) of each of the layers for the frontal bone (left) and parietal bone (right)

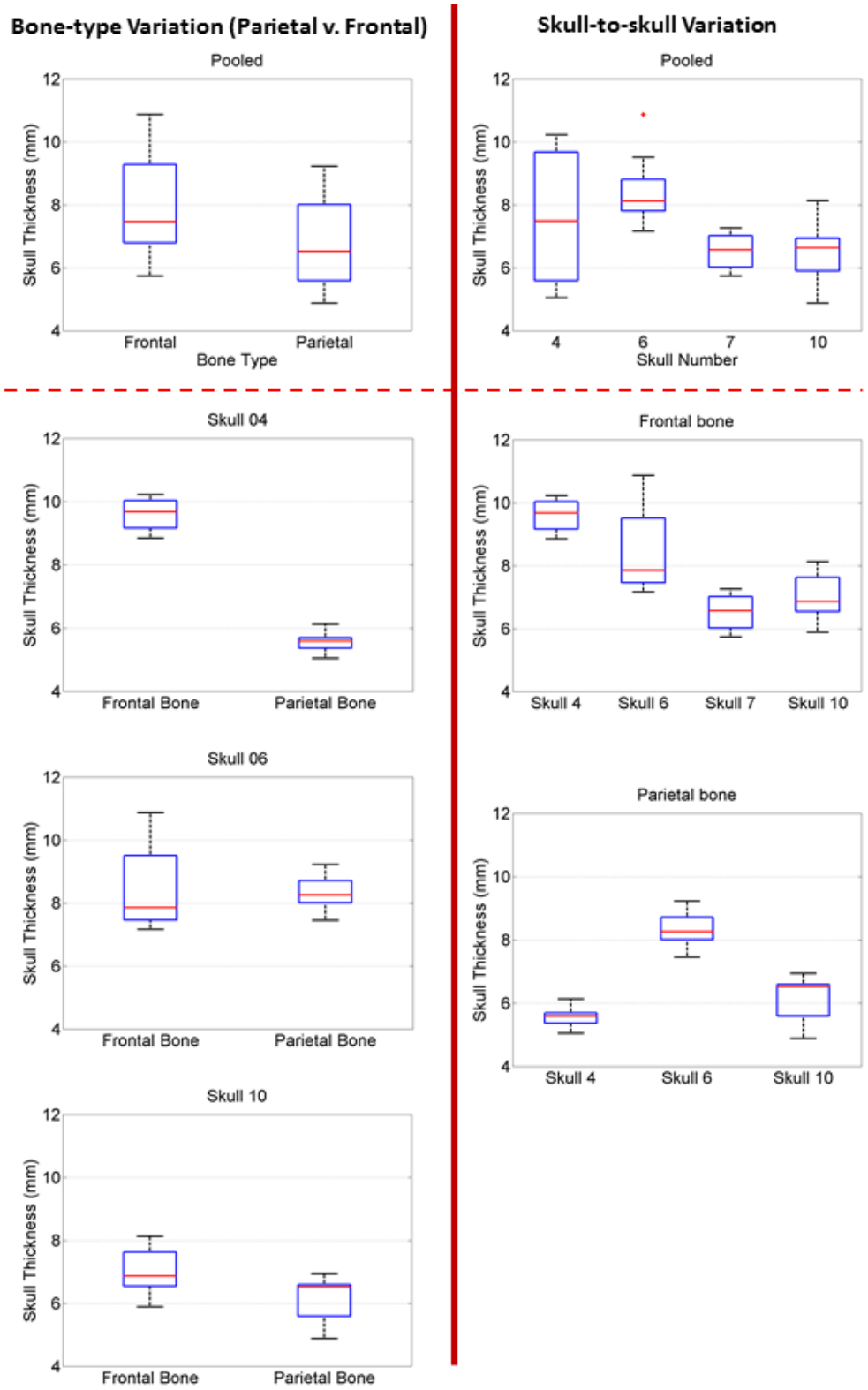

Fig. C-2 Box plots of the total skull thickness (*t*) in mm

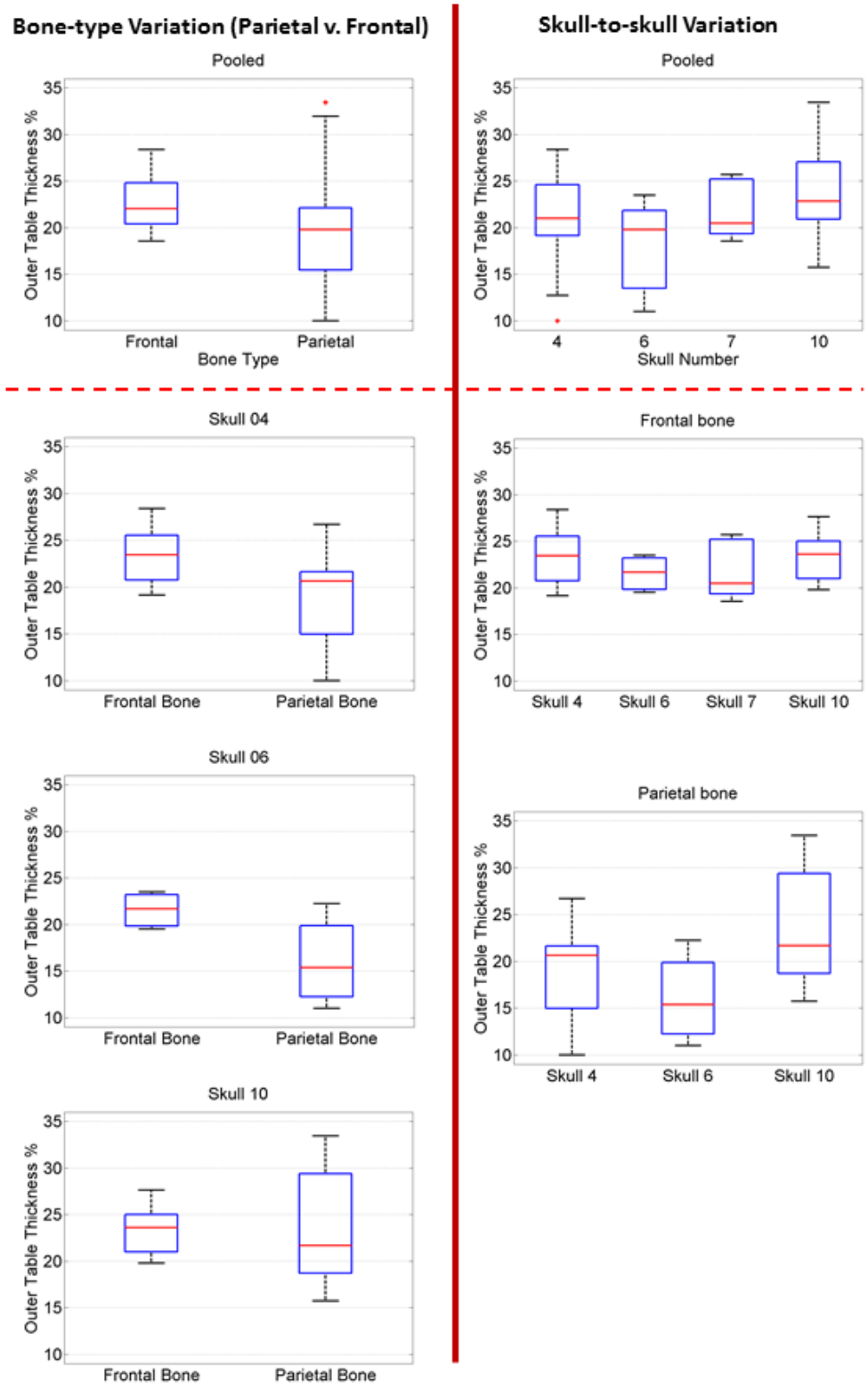

Fig. C-3 Box plots of the thickness percentage of the outer table (t_o)

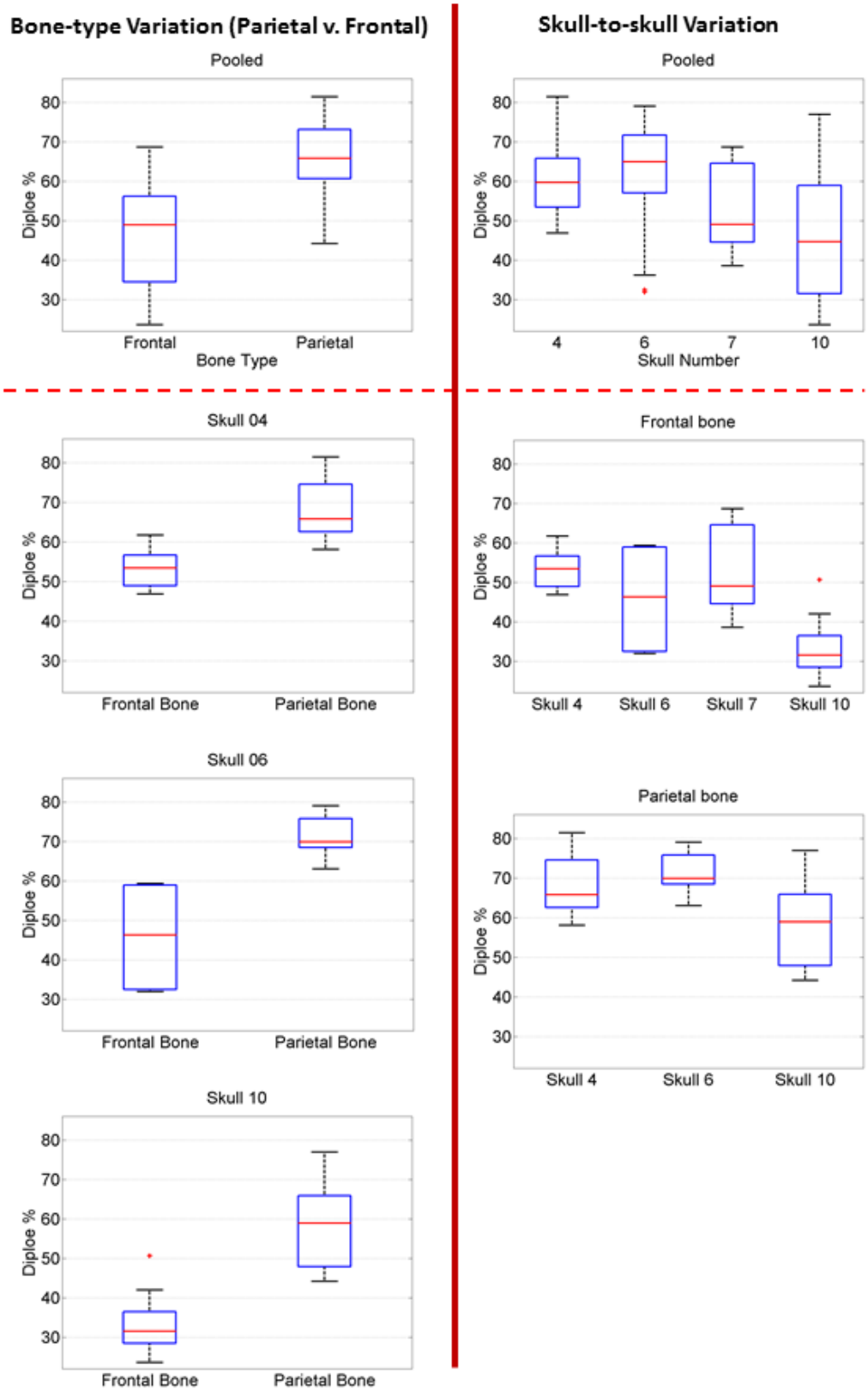

Fig. C-4 Box plots of the thickness percentage of the diploë (t_d)

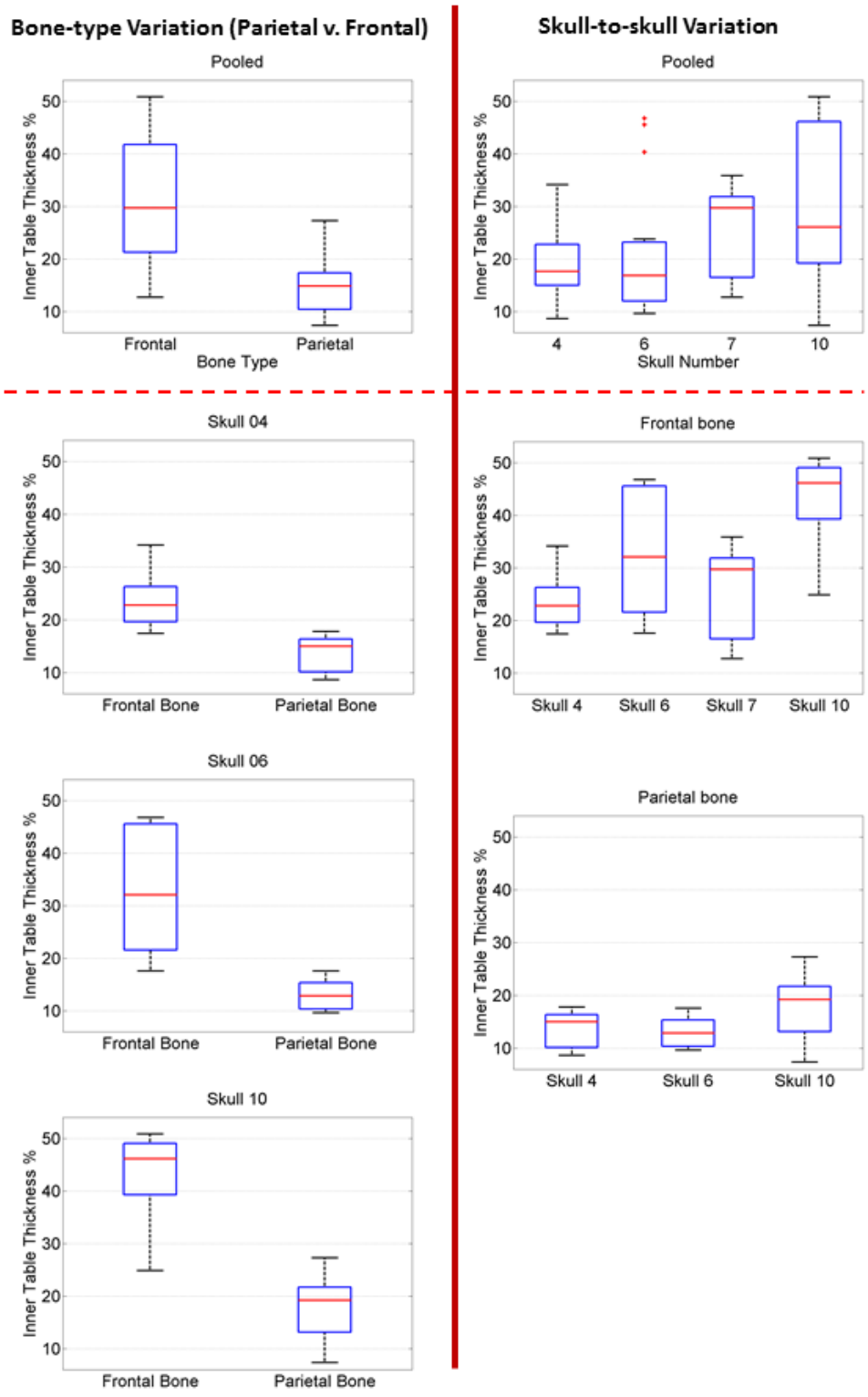

Fig. C-5 Box plots of the thickness percentage of the inner table (t_i)

INTENTIONALLY LEFT BLANK.

Appendix D. Sufficiency of Cross-Sectional Dimensions to Provide Representative Results

In this study, comparison of the porosity-depth profiles across specimens assumed that the amount of variation across the transverse plane was negligible. For this assumption to be applicable, the cross-sectional area (image plane) had to be sufficiently large to provide a true representation of the porosity across the transverse plane. If the imaged area of the specimen was too small, the resulting porosity measurement would be a measure of local variations and not a representative measurement of the bone being studied. This appendix evaluates whether the cross-sectional dimensions that were used were sufficiently large to provide representative measures.

Images with the least amount of bone were believed to be the biggest cause of concern. The extraction grids from the parietal bones of Skulls 10 and 04 had the highest values for peak porosity in the diploë, as also indicated with the corresponding Gaussian coefficient *A* (Table 12). Therefore, for the evaluation of the present appendix, images were extracted from the diploë of 3 specimens from the parietal bone of Skull 10 (10-14, 10-16, and 10-17) and 3 specimens from the parietal bone of Skull 04 (04-14, 04-16, and 04-17). An image was also taken from the frontal bone of Skull 06 (06-05) for comparison, since this bone had the smallest value of peak porosity in the diploë (Table 12).

The image selected from each specimen corresponded to the maximum porosity of the porosity-depth profile, *P(d)*. The images were extracted from the binarized data set (Section 2.2). For each image, a subset of 3 × 3 pixels was seeded in the center of the image. The porosity within the subset was calculated. The subset was then enlarged and the porosity was recalculated. This process was iterated until the subset included the entire image.

The range of porosity (max-min) was measured during the final decade of increments in subset area. This range was less than 2% for all images. Figures D-1–D-7 show the porosity plotted as a function of subset size for each of the images, together with the binary image. These figures indicated that the porosity converged to stable values for all of the images, with the possible exception of Specimens 06-05 (Fig. D-7) and 10-14 (Fig. D-4). The result for Specimen 06-05 was especially surprising. The problem of convergence was expected to be more pronounced for images with less bone area, but Specimen 06-05 had the highest percentage of bone (36.3%).

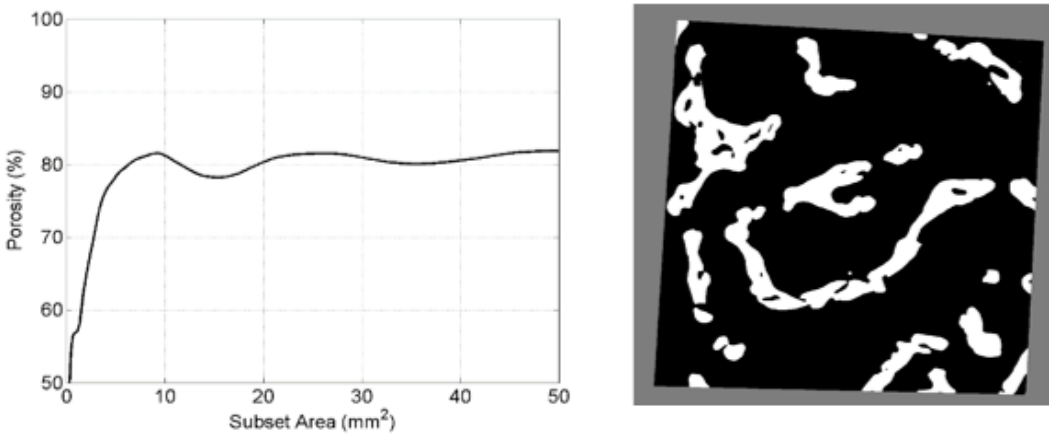

Fig. D-1 Porosity convergence (left) for a cross-sectional image (right) from the diploë of Specimen 04-14

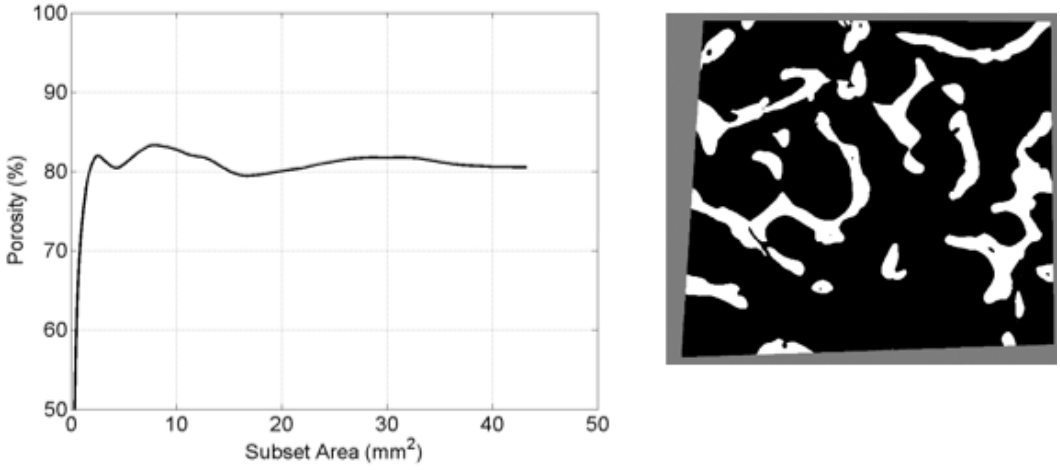

Fig. D-2 Porosity convergence (left) for a cross-sectional image (right) from the diploë of Specimen 04-16

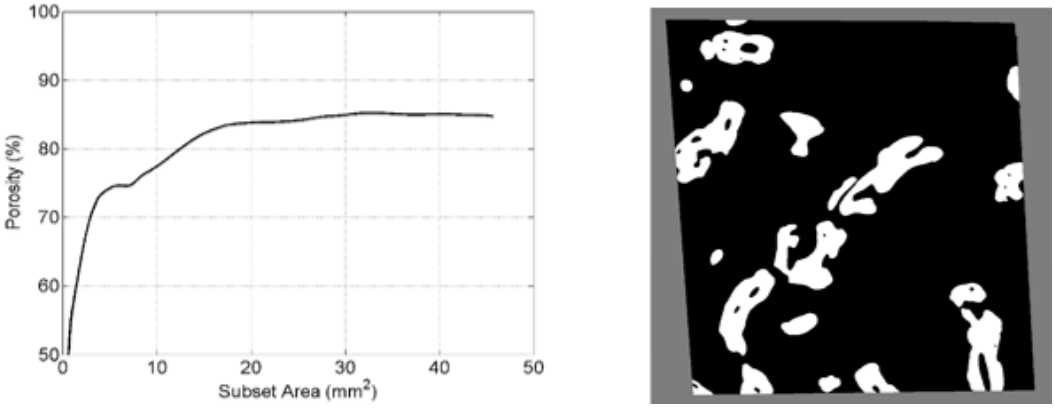

Fig. D-3 Porosity convergence (left) for a cross-sectional image (right) from the diploë of Specimen 04-17

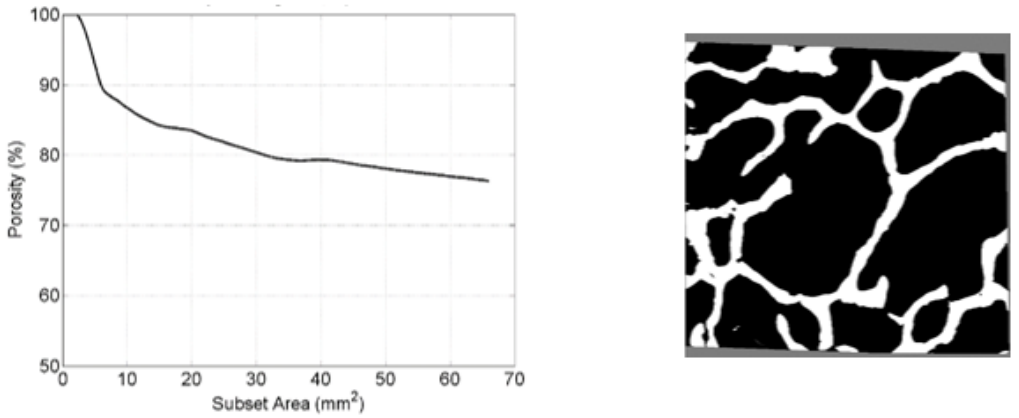

Fig. D-4 Porosity convergence (left) for a cross-sectional image (right) from the diploë of Specimen 10-14

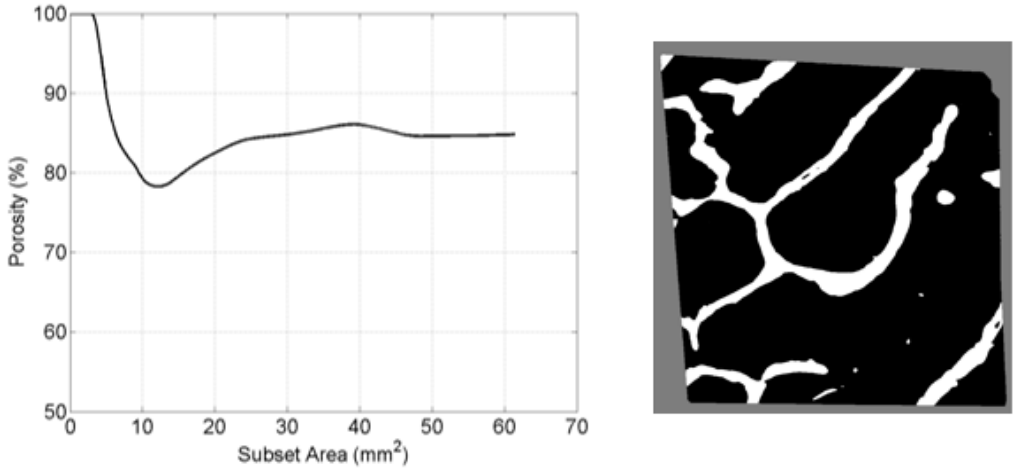

Fig. D-5 Porosity convergence (left) for a cross-sectional image (right) from the diploë of Specimen 10-16

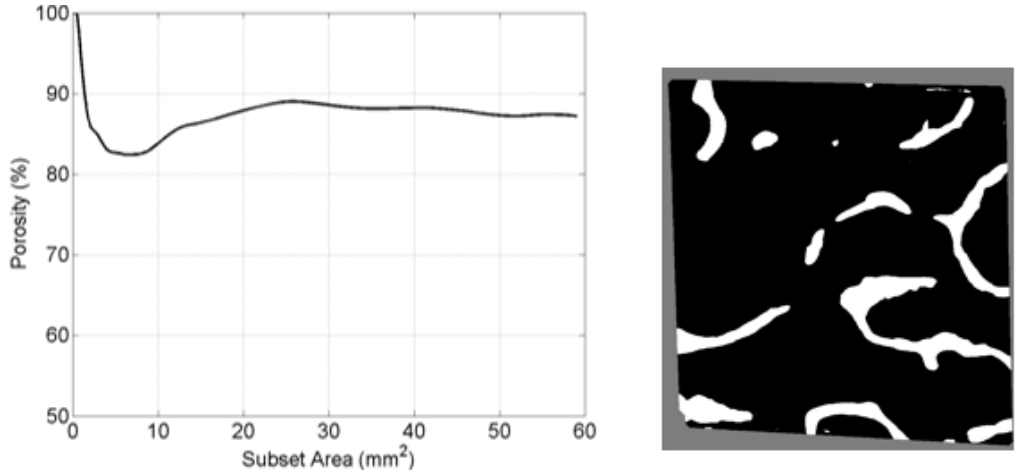

Fig. D-6 Porosity convergence (left) for a cross-sectional image (right) from the diploë of Specimen 10-17

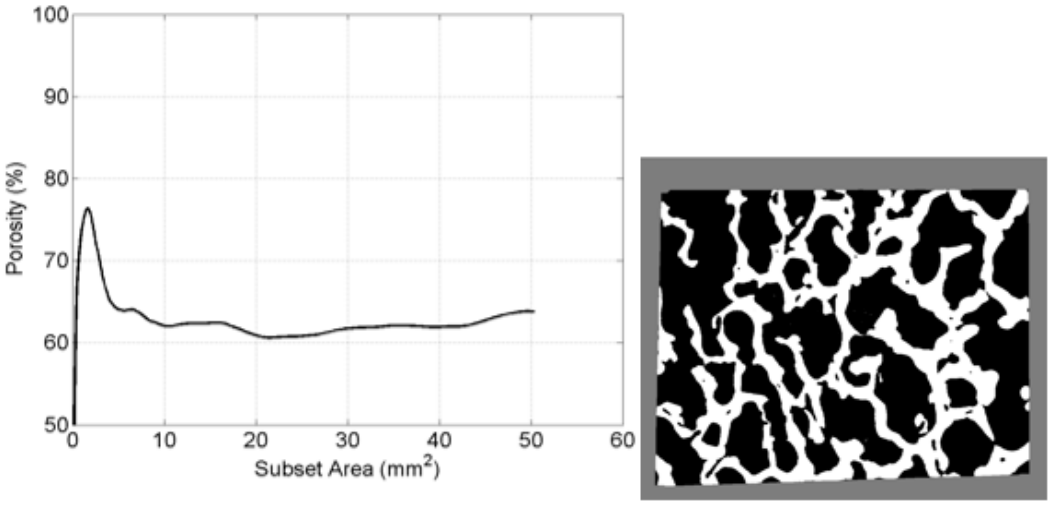

Fig. D-7 Porosity convergence (left) for a cross-sectional image (right) from the diploë of Specimen 06-05

List of Symbols, Acronyms, and Abbreviations

3-D	3-dimensional
ANOVA	analysis of variance
HBSS	Hanks Buffered Saline Solution
HSD	Honestly Significant Difference
fbv	bone-volume-fraction
micro-CT	microcomputed tomography
PMHS	postmortem human subject
ROI	region of interest
VOI	volume of interest

1 (PDF) DEFENSE TECHNICAL INFORMATION CTR DTIC OCA

1 (PDF) DIRECTOR US ARMY RESEARCH LAB IMAL HRA

1 (PDF) DIRECTOR US ARMY RESEARCH LAB RDRL CIO L

1 (PDF) GOVT PRINTG OFC A MALHOTRA

3 (PDF) JOHNS HOPKINS UNIVERSITY T D NGUYEN B NOTGHI S BAILOOR

1 (PDF) INDIAN INST OF TECH R BHARDWAJ

11 (PDF) NATICK SOLDIER RSRCH DEV AND ENG CTR M G CARBONI D COLANTO R DILALLA J FONTECCHIO B KIMBALL J KIREJCZYK J PARKER M MAFEO M MARKEY D PHELPS J WARD

3 (PDF) PROG EXECUTIVE OFC SOLDIER A FOURNIER J MULLENIX J ZHENG

5 (PDF) SOUTHWEST RSRCH INST C ANDERSON JR S CHOCRON D NICOLELLA T HOLMQUIST G JOHNSON

1 (PDF) INST FOR DEFNS ANLYS Y MACHERET

3 (PDF) MRMC DOD BLAST INJURY RSRCH PROGRAM COOR OFC R GUPTA M LEGGIERI R SHOGE

1 (PDF) WIAMAN PMO S MARSH

3 (PDF) MRMC JTAPIC PRGM OFC F LEBEDA W LEI J USCILOWICZ

3 (PDF) US ARMY AEROMEDICAL RSRCH LAB V CHANCEY B MCENTYRE D WISE

1 (PDF) TARDEC R SCHERER

1 (PDF) RDECOM HQ AMSRD PE D RUSIN

44 (PDF) DIR USARL
RDRL SLB W
J GURGANUS
J IVANCIK
W MERMAGEN
K RAFAELS
RDRL WM
S SCHOENFELD
RDRL WMM
M VANLANDINGHAM
RDRL WMM A
D O'BRIEN
T PLAISTED
E WETZEL
RDRL WMM B
T BOGETTI
B LOVE
P MOY
C YEN
RDRL WMM D
S WALSH
B CHEESEMAN
RDRL WMM E
L VARGAS-GONZALEZ

RDRL WMP B
A DAGRO
A DILEONARDI
A EIDSMORE
A GUNNARSSON
C HAMPTON
M KLEINBERGER
J MCDONALD
P MCKEE
S SATAPATHY
K THOMPSON
T WEERASOORIYA
S WOZNIAK
T ZHANG
C HOPPEL
Y HUANG
RDRL WMP C
R BECKER
T BJERKE
A SOKOLOW
RDRL WMP D
R DONEY
B SCOTT
C RANDOW
RDRL WMP E
S BARTUS
M BURKINS
P GILLICH
M LOVE
P SWOBODA
RDRL WMP F
N GNIAZDOWSKI
R GUPTA